

Electron-positron energy deposition rate from neutrino pair annihilation on the rotation axis of neutron and quark stars

Z. Kovács^{*}, K. S. Cheng[†] and T. Harko[‡]

Department of Physics and Center for Theoretical and Computational Physics, The University of Hong Kong,

Pok Fu Lam Road, Hong Kong, Hong Kong SAR, P. R. China

1 October 2010

ABSTRACT

We investigate the deposition of energy due to the annihilations of neutrinos and antineutrinos on the rotation axis of rotating neutron and quark stars, respectively. The source of the neutrinos is assumed to be a neutrino-cooled accretion disk around the compact object. Under the assumption of the separability of the neutrino null geodesic equation of motion we obtain the general relativistic expression of the energy deposition rate for arbitrary stationary and axisymmetric space-times. The neutrino trajectories are obtained by using a ray tracing algorithm, based on numerically solving the Hamilton-Jacobi equation for neutrinos by reversing the proper time evolution. We obtain the energy deposition rates for several classes of rotating neutron stars, described by different equations of state of the neutron matter, and for quark stars, described by the MIT bag model equation of state and in the CFL (Color-Flavor-Locked) phase, respectively. The electron-positron energy deposition rate on the rotation axis of rotating neutron and quark stars is studied for two accretion disk models (isothermal disk and accretion disk in thermodynamical equilibrium). Rotation and general relativistic effects modify the total annihilation rate of the neutrino-antineutrino pairs on the rotation axis of compact stellar, as measured by an observer at infinity. The differences in the equations of state for neutron and quark matter also have important effects on the spatial distribution of the energy deposition rate by neutrino-antineutrino annihilation.

Key words: neutrinos: dense matter – equation of state: stars: rotation: relativity.

1 INTRODUCTION

The neutrino-antineutrino annihilation into electrons and positrons is an important candidate to explain the energy source of the gamma ray bursts (GRBs) (Paczynski 1990; Mészáros & Rees 1992; Ruffert & Janka 1998; Ruffert & Janka 1999; Asano & Iwamoto 2002). The study of the electron energy deposition rate from the $\nu + \bar{\nu} \rightarrow e^+ + e^-$ neutrino annihilation reaction was initiated by Cooperstein et al. (1986), Cooperstein et al. (1987), and Goodman et al. (1987), respectively, and this process has been intensively investigated in the physical and astrophysical literature. Neutrino-antineutrino annihilation into electrons and positrons can deposit more than 10^{51} ergs above the neutrino-sphere of a type II supernova (Goodman et al. 1987). For a full understanding of the effects of the neutrino annihilation in strong gravitational fields, general relativistic effects must be taken into account (Salmonson & Wilson 1999). In a Schwarzschild geometry, the efficiency of the $\nu + \bar{\nu} \rightarrow e^+ + e^-$ process is enhanced over the Newtonian values up to a factor of more than 4, in the regime applicable to Type II supernovae, and by up to a factor of 30 for collapsing neutron stars (Salmonson & Wilson 1999). The neutrino pair annihilation rate into electron pairs between two neutron stars in a binary system was calculated by Salmonson & Wilson (2001).

The gravitational effects on neutrino pair annihilation near the neutrinosphere and around the thin accretion disk were considered in Asano & Fukuyama (2000), by assuming that the accretion disk is isothermal, and that the gravitational field is dominated by the Schwarzschild black hole. General relativistic effects were studied only near the rotation axis. Using idealized models of the accretion disk, Asano & Fukuyama (2001) investigated the relativistic effects on the energy deposition rate via neutrino pair annihilation near the rotation axis of a Kerr black hole, by assuming that the neutrinos are emitted from the accretion disk. The Kerr parameter, a , affects not only the behavior of the neutrinos, but also the inner radius of the accretion disk. When the deposition energy is mainly contributed by the neutrinos coming from the central part, the redshift effect becomes dominant as a

* E-mail: zkovacs@mpifr-bonn.mpg.de

† E-mail: hrspsc@hkucc.hku.hk

‡ E-mail: harko@hkucc.hku.hk

becomes large, and the energy deposition rate is reduced. On the other hand, for a small a , the bending effect becomes dominant and makes the energy increase by factor of 2, as compared with the case that neglects the relativistic effects (Asano & Fukuyama 2001).

General relativity and rotation cause important differences in the spatial distribution of the energy deposition rate by neutrino ν and antineutrino $\bar{\nu}$ -annihilation (Birkel et al. 2007). The energy-momentum deposition rate (MDR) from the $\nu - \bar{\nu}$ collisions above a rotating black hole/thin accretion disk system was calculated by Miller et al. (2003), by imaging the accretion disk at a specified observer using the full geodesic equations, and calculating the cumulative MDR from the scattering of all pairs of neutrinos and antineutrinos arriving at the observer. The dominant contribution to the MDR comes from near the surface of the disk with a tilt of approximately $\pi/4$ in the direction of the disk's rotation. The MDR at large radii is directed outward in a conic section centered around the symmetry axis and is larger by a factor of 10-20 than the on-axis values. There is also a linear dependence of the MDR on the black hole angular momentum. The deposition of energy and momentum, due to the annihilation of neutrinos ν and antineutrinos $\bar{\nu}$ in the vicinity of steady, axisymmetric accretion tori around stellar-mass black holes was investigated in Birkel et al. (2007). The influence of general relativistic effects were analyzed in combination with different neutrinosphere properties and spatial distribution of the energy deposition rate. Assuming axial symmetry, the annihilation rate 4-vector was numerically computed. As compared to Newtonian calculations, general relativistic effects increase the total annihilation rate measured by an observer at infinity by a factor of two when the neutrinosphere is a thin disk, but the increase is only 25% for toroidal and spherical neutrinospheres. Thin disk models yield the highest energy deposition rates for neutrino-antineutrino annihilation, and spherical neutrinospheres the lowest ones, independently of whether general relativistic effects are included or not.

The study of the structure of neutron star disks based on the two-region (i.e., inner and outer) disk scenario was performed by Zhang & Dai (2009), who calculated the neutrino annihilation luminosity from the disk in various cases. As compared with the black hole disk, the neutrino annihilation luminosity above the neutron star disk is higher. The neutron star disk with the advection-dominated inner disk could produce the highest neutrino luminosity, while the disk with an outflow has the lowest (Zhang & Dai 2009). A detailed general relativistic calculation of the neutrino path for a general metric describing a rotating star was studied in Mallick & Majumder (2009). The minimum photosphere radius was calculated

for stars with two different equations of state, each rotating with two different velocities. The results show that the minimum photosphere radius for the hadronic star is greater than for the quark star, and that the minimum photosphere radius increases as the rotational velocity of the star decreases. The minimum photosphere radius along the polar plane is larger than that along the equatorial plane. The estimate of the energy deposition rate for neutrino pair annihilation for the neutrinos coming from the equatorial plane of a rotating neutron star was calculated along the rotation axis in Bhattacharyya et al. (2009), by using the Cook-Shapiro-Teukolsky metric. The neutrino trajectories, and hence the neutrino emitted from the disk, are affected by the redshift due to the disk rotation and gravitation. The energy deposition rate is very sensitive to the value of the temperature, and its variation along the disk. The rotation of the star has a negative effect on the energy deposition rate, it decreases with increase in rotational velocity. A phase transition during a supernova explosion can induce stellar collapse and result in large amplitude stellar oscillations (Chan et al. 2009). Extremely intense pulsating neutrino fluxes, with submillisecond period and with neutrino energy (greater than 30 MeV), can be emitted because the oscillations of the temperature and density are out of phase almost 180° . The dynamical evolution of a phase-transition-induced collapse of a neutron star to a hybrid star, which consists of a mixture of hadronic matter and strange quark matter, was studied in Cheng et al. (2009). It was found that both the temperature and the density at the neutrinosphere are oscillating with acoustic frequency. Consequently, extremely intense, pulsating neutrino/antineutrino fluxes will be emitted periodically. Since the energy and density of neutrinos at the peaks of the pulsating fluxes are much higher than the non-oscillating case, the electron/positron pair creation rate can be enhanced significantly. Some mass layers on the stellar surface can be ejected, by absorbing energy of neutrinos and pairs. These mass ejecta can be further accelerated to relativistic speeds by absorbing electron/positron pairs, created by the neutrino and antineutrino annihilation outside the stellar surface.

It is the purpose of the present paper to consider a comparative systematic study of the neutrino-antineutrino annihilation process on the rotation axis of rotating neutron and strange stars, respectively, and to obtain the basic physical parameters characterizing this process (the electron-positron energy deposition rate per unit volume and unit time), by taking into account the full general relativistic corrections. The source of the neutrinos is assumed to be the accretion disk that can be formed around neutron and quark stars (Zhang & Dai 2009). Neutrino-cooled accretion disks around stellar mass black

holes or neutron stars are plausible candidates for the central engine of gamma-ray bursts (Zhang & Dai 2009). As a first step in obtaining the electron-positron energy deposition rate on the rotation axis of different types of neutron and quark stars we generalize the relativistic description of the neutrino-antineutrino annihilation process to the case of arbitrary stationary and axisymmetric geometries. By assuming that the neutrinos move on null geodesics, the main kinematic parameter of the collision process (the scalar product of the four momenta of the colliding $\nu\bar{\nu}$ pairs) are derived under the assumption that, similarly to the case of the Kerr black holes, the geometric variable in the geodesic equation of motion for the neutrinos can be separated. The domain of validity of this assumption is carefully investigated, and it is shown that in the case of the low mass stellar models with masses around $M = 1.8M_{\odot}$, the error is under 0.5% for angular velocities of the order of $2 \times 10^3 \text{s}^{-1}$, while it is more the 1% for angular velocities higher than $4 \times 10^3 \text{s}^{-1}$. The electron energy deposition rate is calculated for a general axisymmetric metric under the separability assumption. The neutrino trajectories are studied by using a ray tracing algorithm, based on numerically solving the Hamilton-Jacobi equation for neutrinos by reversing the proper time evolution. The electron-positron energy deposition rate on the rotation axis of rotating neutron and quark stars is studied for two accretion disk models (isothermal disk and accretion disk in thermodynamical equilibrium). In all these cases the electron energy deposition rate is obtained for different equations of state of the neutron and quark matter, as well as for different physical parameters of the stars.

In order to compute the electron-positron energy deposition rate, the metric outside the rotating general relativistic stars must be determined. In the present study we obtain the equilibrium configurations of the rotating neutron and quark stars by using the RNS code, as introduced in (Stergioulas & Friedman 1995), and discussed in detail in (Stergioulas 2003). This code was used for the study of different models of rotating neutron stars in (Nozawa et al. 1998) and for the study of the rapidly rotating strange stars (Stergioulas et al. 1999). The software provides the metric potentials for various types of compact rotating general relativistic objects, which can be used to obtain the electron-positron energy deposition rate on the rotation axis of rotating neutron and quark stars.

The present paper is organized as follows. In Section 2 we present the basic formalism for the calculation of the kinematic parameters (four-momenta) of the neutrino-antineutrino annihilation. The general relativistic energy deposition rate is obtained in Section 3. The equations of state of dense neutron and quark matter used in the present study are presented

in Section 4. In Section 5 we obtain the electron-positron energy deposition rates on the rotation axis of the considered classes of neutron and quark stars by assuming that the disk is isothermal. The case of the disk in thermodynamic equilibrium is discussed in Section 6. We discuss and conclude our results in Section 7.

2 FOUR-MOMENTA OF MASSLESS PARTICLES AT THE ROTATIONAL AXIS IN STATIONARY AND AXISYMMETRIC SPACETIMES

Let us consider in the coordinate system (t, r, θ, ϕ) an arbitrary stationary and axially symmetric spacetime, given by the metric

$$ds^2 = c^2 g_{tt} dt^2 + c g_{t\phi} dt d\phi + g_{rr} dr^2 + g_{\theta\theta} d\theta^2 + g_{\phi\phi} d\phi^2, \quad (1)$$

and adapted to the symmetries of the geometry, with the time- and space-like Killing vector fields $(\partial/\partial t)$ and $(\partial/\partial \phi)$, respectively. In the adapted coordinate system the metric coefficients depend only on the coordinates r and θ , measuring the curvature, isotropic, quasi-isotropic etc. radial distances, and the poloidal angle, respectively.

For massless particles propagating along null geodesics in the spacetime (1), the geodesic equations containing the time-derivatives $\dot{r} = g^{rr} p_r$ and $\dot{\theta} = g^{\theta\theta} p_\theta$ can be written as

$$g^{rr} p_r^2 + g^{\theta\theta} p_\theta^2 = \frac{g_{\phi\phi}(\omega_0/c)^2 + 2g_{t\phi}(\omega_0/c)L + g_{tt}L^2}{g_{t\phi}^2 - g_{tt}g_{\phi\phi}}, \quad (2)$$

with the constants of motion $p_t = -\omega_0/c$ and $p_\phi = L$. Here p_t, p_r, p_θ and p_ϕ are the covariant components of the 4-momentum \mathbf{p} of the light like particles. By applying the formal representations

$$g^{rr} g_{\theta\theta} = g_{\theta\theta}/g_{rr} = f(r), \quad (3)$$

$$\frac{g_{\phi\phi} g_{\theta\theta}}{g_{t\phi}^2 - g_{tt} g_{\phi\phi}} = \frac{g^2(r)}{f(r)} - a^2 \sin^2 \theta, \quad (4)$$

$$\frac{g_{t\phi} g_{\theta\theta}}{g_{t\phi}^2 - g_{tt} g_{\phi\phi}} = a - \frac{g(r)h(r, \theta)}{f(r)}, \quad (5)$$

$$\frac{g_{tt} g_{\theta\theta}}{g_{t\phi}^2 - g_{tt} g_{\phi\phi}} = \frac{h^2(r, \theta)}{f(r)} - \frac{1}{\sin^2 \theta}, \quad (6)$$

Eq. (2) can be written as

$$f p_r^2 + p_\theta^2 = \frac{1}{f} \left(g \frac{\omega_0}{c} - h L \right)^2 - \left(a \frac{\omega_0}{c} \sin \theta - \frac{L}{\sin \theta} \right)^2. \quad (7)$$

In Eqs. (3)-(6) we have introduced a constant a , and the functions $f = f(r)$, $g = g(r)$ and $h = h(r, \theta)$, and we have assumed that h depends on both r and θ , but f and g are only

functions of the radial coordinate. This is a rather strong assumption, since these functions are constructed from the metric coefficients via Eqs. (3)-(6), which for a general stationary and axially symmetric spacetime depend on both r and θ ,

$$g_{\pm} = -\frac{1}{g_{tt}} \left[g_{t\phi} h \pm \sqrt{\frac{f}{\sin^2 \theta} (g_{t\phi}^2 - g_{tt} g_{\phi\phi})} \right], \quad (8)$$

$$h^2 = \frac{g_{\theta\theta}}{g_{rr}} \left(\frac{g_{tt} g_{\theta\theta}}{g_{t\phi}^2 - g_{tt} g_{\phi\phi}} + \frac{1}{\sin^2 \theta} \right). \quad (9)$$

We will examine the validity of these assumptions for the neutron and quark star spacetimes under our study in Appendix A. In the following we assume that $g(r) \approx g_+(r, 0)$ is a good approximation for the function g . By virtue of the pure radial dependence of f and h , the geodesic equation (7) for $L = 0$ can be separated with respect to the coordinates r and θ :

$$p_r^2 = \left(\frac{g_+ \omega_0}{f c} \right)^2 - \frac{J^2}{f}, \quad (10)$$

$$p_\theta^2 = - \left(a \frac{\omega_0}{c} \sin \theta \right)^2 + J^2, \quad (11)$$

where J is a separation constant. In the following we use the positive branch g_+ of Eq. (8), which gives $r^2 + a^2$ for the Kerr metric, where a becomes the rotational parameter, and leads to consistent identities in the decompositions in Eqs. (4) and (5). If we insert the expressions for p_r and p_θ given by Eqs. (10) and (11) into the scalar product of the 4-momenta of a scattering $\nu\bar{\nu}$ pair for $L = 0$ we obtain

$$\begin{aligned} \mathbf{p}_\nu \cdot \mathbf{p}_{\bar{\nu}} &= g^{tt} \frac{\omega_{0\nu}}{c} \frac{\omega_{0\bar{\nu}}}{c} + g^{rr} p_{\nu r} p_{\bar{\nu} r} + g^{\theta\theta} p_{\nu\theta} p_{\bar{\nu}\theta} \\ &= \frac{\omega_{0\nu}}{c} \frac{\omega_{0\bar{\nu}}}{c} g^{tt} + g^{rr} \frac{g_+^2}{f^2} \frac{\omega_{0\nu}}{c} \frac{\omega_{0\bar{\nu}}}{c} \sqrt{1 - \frac{f}{g_+^2} \frac{c J_\nu^2}{\omega_{0\nu}}} \sqrt{1 - \frac{f}{g_+^2} \frac{c J_{\bar{\nu}}^2}{\omega_{0\bar{\nu}}}} \\ &\quad + g^{\theta\theta} \frac{\omega_{0\nu}}{c} \frac{\omega_{0\bar{\nu}}}{c} \sqrt{\frac{c^2 J_\nu^2}{\omega_{0\nu}^2} - a^2 \sin^2 \theta} \sqrt{\frac{c^2 J_{\bar{\nu}}^2}{\omega_{0\bar{\nu}}^2} - a^2 \sin^2 \theta}. \end{aligned}$$

By introducing the variable ρ_ν , and the horizontal collision angle θ_ν

$$\rho_\nu = \frac{c J_\nu}{\omega_{0\nu}}, \quad \sin \theta_\nu = \frac{\sqrt{f}}{g_+} \rho_\nu,$$

we can cast the result in the form

$$\mathbf{p}_\nu \cdot \mathbf{p}_{\bar{\nu}} = \frac{\omega_{0\nu} \omega_{0\bar{\nu}}}{c^2} \left(g^{tt} + g^{\theta\theta} \frac{g_+^2}{f} \cos \theta_\nu \cos \theta_{\bar{\nu}} + g^{\theta\theta} \sqrt{\frac{g_+^2}{f} \sin^2 \theta_\nu - a^2 \sin^2 \theta} \sqrt{\frac{g_+^2}{f} \sin^2 \theta_{\bar{\nu}} - a^2 \sin^2 \theta} \right).$$

In the following we restrict our study to the neutrino-anti neutrino pairs that are scattering at the rotational axis. For $\theta = 0$ the scalar product reduces to the expression

$$\mathbf{p}_\nu \cdot \mathbf{p}_{\bar{\nu}} = \frac{\omega_{0\nu} \omega_{0\bar{\nu}}}{c^2} \left[g^{tt} + g^{\theta\theta} \left(\frac{g_+^2}{f} \cos \theta_\nu \cos \theta_{\bar{\nu}} + \frac{g_+^2}{f} \sin \theta_\nu \sin \theta_{\bar{\nu}} \right) \right]$$

$$= -\frac{\omega_{0\nu}\omega_{0\bar{\nu}}}{c^2}g^{\theta\theta}\frac{g_+^2}{f}[1 - \cos\theta_\nu \cos\theta_{\bar{\nu}} - \sin\theta_\nu \sin\theta_{\bar{\nu}}],$$

where we have used the relation $g^{tt} = -g_{\phi\phi}/(g_{t\phi}^2 - g_{tt}g_{\phi\phi})$ and Eq. (4), evaluated at $\theta = 0$.

By introducing the proper energy of the neutrinos defined as

$$\varepsilon_\nu = \hbar\omega_{0\nu} \sqrt{\frac{g_{\phi\phi}}{g_{t\phi}^2 - g_{tt}g_{\phi\phi}}}\bigg|_{\theta=0} = \hbar\omega_{0\nu} \sqrt{g^{\theta\theta}(r, 0)\frac{g_+^2(r, 0)}{f(r)}},$$

we obtain

$$\mathbf{p}_\nu \cdot \mathbf{p}_{\bar{\nu}} = -\frac{\varepsilon_\nu \varepsilon_{\bar{\nu}}}{c^2}(1 - \cos\theta_\nu \cos\theta_{\bar{\nu}} - \sin\theta_\nu \sin\theta_{\bar{\nu}}), \quad (12)$$

or, in the general case,

$$\mathbf{p}_\nu \cdot \mathbf{p}_{\bar{\nu}} = -\frac{\varepsilon_\nu \varepsilon_{\bar{\nu}}}{c^2}[1 - \cos\theta_\nu \cos\theta_{\bar{\nu}} - \sin\theta_\nu \sin\theta_{\bar{\nu}} \cos(\varphi_\nu - \varphi_{\bar{\nu}})], \quad (13)$$

where φ_ν and $\varphi_{\bar{\nu}}$ are the azimuthal collision angles for the $\nu\bar{\nu}$ pair, as measured at the rotational axis.

This equation is the same as the one derived for the Kerr spacetime (Asano & Fukuyama 2001). Provided that neglecting the angular dependence of the function g_+ , and the substitution of the separated geodesic equations (10) and (11) into the scalar product does not increase the error propagation significantly, the expression (13) is a good approximation for any stationary and axially symmetric spacetime. We can therefore use the same procedure to calculate the neutrino-antineutrino annihilation energy deposition rate at the rotational axis of neutron and quarks stars as the one used for the black holes.

3 ENERGY DEPOSITION RATE FROM $\nu\bar{\nu}$ PAIR ANNIHILATION ALONG THE ROTATIONAL AXIS

We consider a geometrically thin accretion disk around a rotating compact object, with an inner edge at the curvature radius R_{in} , and a cutoff radius at R_{out} . We assume that the mass-energy of the disk produces only a negligible effect on the spacetime geometry of the central object. Thus any massless particle can propagate along null geodesics in the vicinity of the disk-compact object system, with the global geometry determined by the central massive object. We also suppose that the disk is the primary source of neutrinos in the system, and we neglect any interaction between the disk and the neutrino/anti neutrino radiation after their generation in the rotating plasma. Furthermore we assume that these particles can freely propagate along null geodesics even in the interior of the central object, and have only negligible energy losses in the interactions with the stellar matter. In the

following we determine the electron-positron energy deposition rate (EDR) produced due to the neutrino-anti neutrino pair annihilations into e^-e^+ pairs along the rotation axis of the compact object, where the baryon contamination related to the matter content of the disk corona is minimal.

For any point $\mathbf{r} = (r, \theta, \phi)$ of the $\nu - \bar{\nu}$ collision, the EDR per unit volume via electron-positron pair creation due to neutrino-anti neutrino annihilation is given by

$$\dot{q}(\mathbf{r}) = \frac{dE_0}{dtdV} = \int \int f_\nu(\mathbf{p}_\nu, \mathbf{r}) f_{\bar{\nu}}(\mathbf{p}_{\bar{\nu}}, \mathbf{r}) \{ \sigma_{\nu\bar{\nu}} |\mathbf{v}_\nu - \mathbf{v}_{\bar{\nu}}| \varepsilon_\nu \varepsilon_{\bar{\nu}} \} \frac{\varepsilon_\nu + \varepsilon_{\bar{\nu}}}{\varepsilon_\nu \varepsilon_{\bar{\nu}}} d^3\mathbf{p}_\nu d^3\mathbf{p}_{\bar{\nu}}, \quad (14)$$

where \mathbf{p}_ν and $\mathbf{p}_{\bar{\nu}}$ are the 3-momenta in the momentum space, f_ν and $f_{\bar{\nu}}$ are the neutrino and anti-neutrino number densities, and \mathbf{v}_ν , ε_ν , $\mathbf{v}_{\bar{\nu}}$ and $\varepsilon_{\bar{\nu}}$ are the 3-velocities and the energy of the colliding neutrino-antineutrino pairs, respectively (Goodman et al. 1987). The cross-section of the collision is denoted by $\sigma_{\nu\bar{\nu}}$, and can be calculated by using the formula

$$\sigma_{\nu\bar{\nu}} = KG_F^2(\varepsilon_\nu \varepsilon_{\bar{\nu}} - c^2 \mathbf{p}_\nu \cdot \mathbf{p}_{\bar{\nu}}) = -KG_F^2 \mathbf{p}_\nu \cdot \mathbf{p}_{\bar{\nu}}$$

(special relativity is considered), where $K = (1 \pm 4 \sin^2 \theta_W + 8 \sin^4 \theta_W)/6\pi$, with $\sin^2 \theta_W = 0.23$, and $G_F^2 = 5.29 \times 10^{-44} \text{ cm}^2 \text{ MeV}^{-2}$, respectively. By applying the decompositions $\mathbf{p}_\nu = \varepsilon_\nu \boldsymbol{\Omega}_\nu$ and $d^3\mathbf{p}_\nu = \varepsilon_\nu^2 d\varepsilon_\nu d\boldsymbol{\Omega}_\nu$, with the solid angle vector $\boldsymbol{\Omega}_\nu$ pointing in the direction of \mathbf{p}_ν , and with the assumption that the neutrino source in the disk emits particles isotropically, the integral in Eq. (14) can be separated into an energy integral and an angular part.

After evaluating the energy integral for fermions and inserting the general relativistic version of the scalar product of the 4-momenta given by Eq. (13) into the cross-section equation for the colliding $\nu\bar{\nu}$ pair, for a stationary and axially symmetric geometry we obtain the EDR at the rotational axis ($\theta = 0$) per unit volume per unit time ($dtdV = \sqrt{-g}d^4x$) in the form (Asano & Fukuyama 2001)

$$\begin{aligned} \dot{q}(r) &= \frac{dE_0}{dtdV} = 2cKG_F^2 \Theta(r) \int \int f_\nu f_{\bar{\nu}} (\varepsilon_\nu + \varepsilon_{\bar{\nu}}) \varepsilon_\nu^3 \varepsilon_{\bar{\nu}}^3 d\varepsilon_\nu d\varepsilon_{\bar{\nu}} \\ &= \frac{21\pi^4}{4} \zeta(5) \frac{KG_F^2}{h^6 c^5} k^9 T_{eff}^9(3r_g) \Theta(r). \end{aligned} \quad (15)$$

Here $T_{eff}(3r_g)$ is the effective neutrino temperature evaluated at $3 \times r_g = 6GM/c^2$, and ζ is the Riemann zeta function. The angular part $\Theta(r)$ of the EDR is given by

$$\begin{aligned} \Theta(r) &= \frac{1}{T_{eff}^9(3r_g)} \left(\frac{g_{\phi\phi}}{g_{t\phi}^2 - g_{tt}g_{\phi\phi}} \Big|_{\theta=0} \right)^4 \int_{\theta_m}^{\theta_M} d\theta_\nu \sin \theta_\nu \\ &\times \int_{\theta_m}^{\theta_M} d\theta_{\bar{\nu}} \sin \theta_{\bar{\nu}} \int_0^{2\pi} d\varphi_\nu \int_0^{2\pi} d\varphi_{\bar{\nu}} T_0^5(R_\nu) \\ &\times T_0^4(R_{\bar{\nu}}) [1 - \sin \theta_\nu \sin \theta_{\bar{\nu}} \cos(\varphi_\nu - \varphi_{\bar{\nu}})] \end{aligned}$$

$$- \cos \theta_\nu \cos \theta_{\bar{\nu}}]^2, \quad (16)$$

with the neutrino temperature T_0 observed at infinity, and the angular boundaries θ_m and θ_M of the collision angle for the (anti)neutrinos arriving from the disk edges at R_{in} and R_{out} , respectively. The expression in parenthesis is the redshift factor for massless particles.

Integrating this expression over the azimuthal collision angles φ_ν and $\varphi_{\bar{\nu}}$ of the neutrino-antineutrino pairs yields the formula

$$\begin{aligned} \Theta(r) = & \frac{2\pi^2}{T_{eff}^9(3r_g)} \left(\frac{g_{\phi\phi}}{g_{t\phi}^2 - g_{tt}g_{\phi\phi}} \Big|_{\theta=0} \right)^4 \left[2 \int_{\mu_m}^{\mu_M} d\mu_\nu T_0^5(\mu_\nu) \int_{\mu_m}^{\mu_M} d\mu_{\bar{\nu}} T_0^4(\mu_{\bar{\nu}}) \right. \\ & + \int_{\mu_m}^{\mu_M} d\mu_\nu (1 - \mu_\nu^2) T_0^5(\mu_\nu) \int_{\mu_m}^{\mu_M} d\mu_{\bar{\nu}} (1 - \mu_{\bar{\nu}}^2) T_0^4(\mu_{\bar{\nu}}) \\ & + 2 \int_{\mu_m}^{\mu_M} d\mu_\nu \mu_\nu^2 T_0^5(\mu_\nu) \int_{\mu_m}^{\mu_M} d\mu_{\bar{\nu}} \mu_{\bar{\nu}}^2 T_0^4(\mu_{\bar{\nu}}) \\ & \left. - 4 \int_{\mu_m}^{\mu_M} d\mu_\nu \mu_\nu T_0^5(\mu_\nu) \int_{\mu_m}^{\mu_M} d\mu_{\bar{\nu}} \mu_{\bar{\nu}} T_0^4(\mu_{\bar{\nu}}) \right], \quad (17) \end{aligned}$$

where $\mu_\nu = \cos \theta_\nu$, $\mu_{\bar{\nu}} = \cos \theta_{\bar{\nu}}$, $\mu_m = \cos \theta_m$ and $\mu_M = \cos \theta_M$.

In order to determine the boundary angles θ_m and θ_M (or, in turn, μ_m and μ_M), we traced the null geodesics back from a given point on the rotational axis to its intersection with the equatorial plane. In the ray tracing code we supplemented the coordinates of r and θ with their momenta p_r and p_θ , and used the dynamical equations for the extended set of variables. We present some details of this method in Appendix B. For a given set of canonical data of the final point at the rotational axis the code derived the canonical data of the initial point in the equatorial plane. That is, for any radial coordinate r along the axis, the code can provide the values of p_θ and p_r for which null geodesics starting from the equatorial plane at a given radius R will hit the axis at r . The collision angle θ_ν is determined by the scalar product of the normal vector pointing into the direction of the 3-momentum $\mathbf{p}_\nu = ((p_\nu)^r, (p_\nu)^\theta, (p_\nu)^\phi)$ of the neutrino passing through the axis, and the normal vector $\mathbf{e}_z = (1/\sqrt{g_{rr}}, 0, 0)$ of the rotational axis,

$$\cos \theta_\nu = \frac{\mathbf{p}_\nu \cdot \mathbf{e}_z}{|\mathbf{p}_\nu|} = \frac{(p_\nu)_r}{\sqrt{g_{rr}[(p_\nu)_r^2/g_{rr} + (p_\nu)_\theta^2/g_{\theta\theta}]}} \quad (18)$$

where we have used the expression $\mathbf{p}_\nu \cdot \mathbf{e}_z = g_{rr}(p_\nu)^r(e_z)^r = \sqrt{g_{rr}}(p_\nu)^r$, and the fact that the norm of the 3-momentum is reduced to $|\mathbf{p}_\nu| = \sqrt{g^{rr}(p_\nu)_r^2 + g^{\theta\theta}(p_\nu)_\theta^2}$, since $(p_\nu)_\phi = L_\nu$ is zero for the particles reaching the rotational axis.

We can express the square of p_r from the geodesic equation (2) as

$$\frac{(p_\nu)_r^2}{g_{rr}} = \frac{g_{\phi\phi}(\omega_0/c)^2}{g_{t\phi}^2 - g_{tt}g_{\phi\phi}} - \frac{(p_\nu)_\theta^2}{g_{\theta\theta}} = \frac{g_+^2(\omega_0/c)^2 f^{-1} - (p_\nu)_\theta^2}{g_{\theta\theta}}. \quad (19)$$

Here the constant of motion ω_0 for the particle energy is arbitrary ($< c^2$), provided the mass shell condition $\mathbf{p}_\nu \cdot \mathbf{p}_\nu = 0$ for null particles holds. Combining Eqs. (18) and (19) together we obtain a relation between the collision angle and p_θ :

$$\cos \theta_\nu = \pm \sqrt{1 - \left[\frac{(p_\nu)_\theta}{\omega_0/c} \right]^2 \frac{f(r)}{g_+^2(r, 0)}} \quad (20)$$

or

$$\sin^2 \theta_\nu = \left[\frac{(p_\nu)_\theta}{\omega_0/c} \right]^2 \frac{f(r)}{g_+^2(r, 0)}. \quad (21)$$

From the latter formula in the Kerr spacetime we have $\sin \theta_\nu = \rho_\nu \sqrt{\Delta}/(r^2 + a^2)$, with the horizon function $\Delta = r^2 + a^2 - 2Mr$, and $\rho_\nu = c(p_\nu)_\theta/\omega_0 = cJ/\omega_0$ at the rotational axis (Asano & Fukuyama 2001). We used the relation (20) to calculate θ_ν for any particle traced back from a given point at r on the rotational axis, with a given value of p_θ , to its starting point at R in the equatorial plane. For $R = R_{in}$ and $R = R_{out}$, Eq. (20) provides the values of θ_m , θ_M (o, equivalently, μ_m and μ_M), for any value of r .

For neutrinos propagating from the accretion disk with zero angular momentum in the direction of the disk rotation, the energy is redshifted by the gravitational potential, and Lorenz boosted due to the disk motion measured in the locally non-rotating frame (LNRF) of the spacetime. Then the observed neutrino temperature can be written as

$$T_0(R) = \frac{\sqrt{g_{t\phi}^2 - g_{tt}g_{\phi\phi}}}{\Gamma g_{\phi\phi}} T_{eff}(R), \quad (22)$$

where $\Gamma = (1 - v^2/c^2)^{-1/2}$, and the square of the disk velocity measured in the LNRF is

$$v^2 = \frac{g_{\phi\phi}^2}{g_{t\phi}^2 - g_{tt}g_{\phi\phi}} (\Omega_K - \omega)^2$$

with the angular frequency Ω_K of the Keplerian disk, and the frame dragging frequency ω of the spacetime given by

$$\Omega_K = \frac{d\phi}{dt} = c \frac{-g_{t\phi,r} + \sqrt{(g_{t\phi,r})^2 - g_{tt,r}g_{\phi\phi,r}}}{g_{\phi\phi,r}}, \quad \omega = -\frac{cg_{t\phi}}{g_{\phi\phi}},$$

respectively. If we solve Eq. (20) for p_θ at a given value of θ_ν , and use the result to prescribe the canonical data of any final point on the axis, then we can trace null particles back to their initial point in the equatorial plane. Hence we can determine the radial coordinate R measured along the disk at which T_0 has to be evaluated in the integral given by Eq. (17) for any $\mu_\nu = \arccos \theta_\nu$.

The energy deposition rate per unit volume for a distant observer is given by Eq. (15), with an integral over the volume $dV = \sqrt{-g} dr d\theta d\phi$. Since we estimate the EDR only along

the rotational axis over r_{min} and r_{max} with $\theta \rightarrow 0$, it is proportional to the integral

$$\begin{aligned} \left. \frac{dE_0}{dt} \right|_{\theta=0} &\simeq 2 \frac{d}{d\theta} \int_0^{2\pi} \int_0^{\pi/2} \int_{r_{min}}^{r_{max}} \frac{dE_0}{dt dV} \sqrt{-g} dr d\theta d\phi \Big|_{\theta=0} \\ &= 21\pi^5 \zeta(5) \frac{K G_F^2}{h^6 c^5} k^9 T_{eff}^9 (3r_g) r_g^2 \int_{r_{min}}^{r_{max}} G(r) dr, \end{aligned} \quad (23)$$

where the dimensionless quantity $G(r)$ is defined by

$$G(r) \equiv r_g^{-2} \left. \frac{\sqrt{-g(r, \theta)}}{\sin \theta} \right|_{\theta=0} \Theta(r). \quad (24)$$

We note that since $g \sim \sin^2 \theta$ holds for the metric determinant of stationary and axially symmetric spacetimes in both the curvature and isotropic coordinate systems, $d\sqrt{-g}/d\theta|_{\theta=0}$ can be written in the form $(\sqrt{-g}/\sin \theta)(d \sin \theta/d\theta)_{\theta=0} = \sqrt{-g}/\sin \theta$, which has a finite value at $\theta = 0$. For Kerr the metric the cofactor of $\Theta(r)$ in the Eq. (24) is just $(r^2 + a^2)/r_g^2$, and G reduces to its definition introduced in (Asano & Fukuyama 2001).

4 EQUATIONS OF STATE AND STELLAR MODELS

In order to obtain a consistent and realistic physical description of the rotating general relativistic neutron and quark stars, as a first step we have to adopt the equations of state for the dense neutron and quark matter, respectively. In the present study we consider the following equations of state for neutron and quark matter:

1) Akmal-Pandharipande-Ravenhall (APR) EOS (Akmal et al. 1998). EOS APR has been obtained by using the variational chain summation methods and the Argonne v_{18} two-nucleon interaction. Boost corrections to the two-nucleon interaction, which give the leading relativistic effect of order $(v/c)^2$, as well as three-nucleon interactions, are also included in the nuclear Hamiltonian. The density range is from 2×10^{14} g/cm³ to 2.6×10^{15} g/cm³. The maximum mass limit in the static case for this EOS is $2.20 M_\odot$. We join this equation of state to the composite BBP ($\epsilon/c^2 > 4.3 \times 10^{11}$ g/cm³) (Baym et al. 1971a) - BPS (10^4 g/cm³ $< 4.3 \times 10^{11}$ g/cm³) (Baym et al. 1971b) - FMT ($\epsilon/c^2 < 10^4$ g/cm³) (Feynman et al. 1949) equations of state, respectively.

2) Douchin-Haensel (DH) EOS (Douchin & Haensel 2001). EOS DH is an equation of state of the neutron star matter, describing both the neutron star crust and the liquid core. It is based on the effective nuclear interaction SLy of the Skyrme type, which is particularly suitable for the application to the calculation of the properties of very neutron rich matter. The structure of the crust, and its EOS, is calculated in the zero temperature approximation,

and under the assumption of the ground state composition. The EOS of the liquid core is calculated assuming (minimal) $npe\mu$ composition. The density range is from 3.49×10^{11} g/cm³ to 4.04×10^{15} g/cm³. The minimum and maximum masses of the static neutron stars for this EOS are $0.094M_{\odot}$ and $2.05M_{\odot}$, respectively.

3) Shen-Toki-Oyamatsu-Sumiyoshi (STOS) EOS (Shen et al. 1998). The STOS equation of state of nuclear matter is obtained by using the relativistic mean field theory with nonlinear σ and ω terms in a wide density and temperature range, with various proton fractions. The EOS was specifically designed for the use of supernova simulation and for the neutron star calculations. The Thomas-Fermi approximation is used to describe inhomogeneous matter, where heavy nuclei are formed together with free nucleon gas. The temperature is mentioned for each STOS equation of state, so that, for example, STOS0 represents the STOS EOS for $T = 0$ MeV. For the proton fraction we chose the value $Y_p = 10^{-2}$ in order to avoid the negative pressure regime for low baryon mass densities.

4) Relativistic Mean Field (RMF) equations of state with isovector scalar mean field corresponding to the δ -meson- RMF soft and RMF stiff EOS (Kubis & Kutschera 1997). While the δ -meson mean field vanishes in symmetric nuclear matter, it can influence properties of asymmetric nuclear matter in neutron stars. The Relativistic mean field contribution due to the δ -field to the nuclear symmetry energy is negative. The energy per particle of neutron matter is then larger at high densities than the one with no δ -field included. Also, the proton fraction of β -stable matter increases. Splitting of proton and neutron effective masses due to the δ -field can affect transport properties of neutron star matter. The equations of state can be parameterized by the coupling parameters $C_{\sigma}^2 = g_{\sigma}^2/m_{\sigma}^2$, $C_{\omega}^2 = g_{\omega}^2/m_{\omega}^2$, $\bar{b} = b/g_{\sigma}^3$ and $\bar{c} = c/g_{\sigma}^4$, where m_{σ} and m_{ω} are the masses of the respective mesons, and b and c are the coefficients in the potential energy $U(\sigma)$ of the σ -field. The soft RMF EOS is parameterized by $C_{\sigma}^2 = 1.582$ fm², $C_{\omega}^2 = 1.019$ fm², $\bar{b} = -0.7188$ and $\bar{c} = 6.563$, while the stiff RMF EOS is parameterized by $C_{\sigma}^2 = 11.25$ fm², $C_{\omega}^2 = 6.483$ fm², $\bar{b} = 0.003825$ and $\bar{c} = 3.5 \times 10^{-6}$, respectively.

5) Baldo-Bombaci-Burgio (BBB) EOS (Baldo et al. 1997). The BBB EOS is an EOS for asymmetric nuclear matter, derived from the Brueckner-Bethe-Goldstone many-body theory with explicit three-body forces. Two EOS's are obtained, one corresponding to the Argonne AV14 (BBBAV14), and the other to the Paris two-body nuclear force (BBBParis), implemented by the Urbana model for the three-body force. The maximum static mass configurations are $M_{max} = 1.8M_{\odot}$ and $M_{max} = 1.94M_{\odot}$ when the AV14 and Paris interactions

are used, respectively. The onset of direct Urca processes occurs at densities $n \geq 0.65 \text{ fm}^{-3}$ for the AV14 potential and $n \geq 0.54 \text{ fm}^{-3}$ for the Paris potential. The comparison with other microscopic models for the EOS shows noticeable differences. The density range is from $1.35 \times 10^{14} \text{ g/cm}^3$ to $3.507 \times 10^{15} \text{ g/cm}^3$.

6) Bag model equation of state for quark matter (Q) EOS (Itoh 1970; Bodmer 1971; Witten 1984; Cheng et al. 1998). For the description of the quark matter we adopt first a simple phenomenological description, based on the MIT bag model equation of state, in which the pressure p is related to the energy density ρ by

$$p = \frac{1}{3}(\rho - 4B)c^2, \quad (25)$$

where B is the difference between the energy density of the perturbative and non-perturbative QCD vacuum (the bag constant), with the value $4B = 4.2 \times 10^{14} \text{ g/cm}^3$.

7) It is generally agreed today that the color-flavor-locked (CFL) state is likely to be the ground state of matter, at least for asymptotic densities, and even if the quark masses are unequal (Alford et al. 1999; Rapp et al. 2000; Horvath & Lugones 2004; Alford et al. 2007). Moreover, the equal number of flavors is enforced by symmetry, and electrons are absent, since the mixture is automatically neutral. By assuming that the mass m_s of the s quark is not large as compared to the chemical potential μ , the thermodynamical potential of the quark matter in CFL phase can be approximated as (Lugones & Horvath 2002)

$$\Omega_{CFL} = -\frac{3\mu^4}{4\pi^2} + \frac{3m_s^2}{4\pi^2} - \frac{1 - 12 \ln(m_s/2\mu)}{32\pi^2} m_s^4 - \frac{3}{\pi^2} \Delta^2 \mu^2 + B, \quad (26)$$

where Δ is the gap energy. With the use of this expression the pressure P of the quark matter in the CFL phase can be obtained as an explicit function of the energy density ε in the form (Lugones & Horvath 2002)

$$P = \frac{1}{3}(\varepsilon - 4B) + \frac{2\Delta^2 \delta^2}{\pi^2} - \frac{m_s^2 \delta^2}{2\pi^2}, \quad (27)$$

where

$$\delta^2 = -\alpha + \sqrt{\alpha^2 + \frac{4}{9}\pi^2(\varepsilon - B)}, \quad (28)$$

and $\alpha = -m_s^2/6 + 2\Delta^2/3$. In the following the value of the gap energy Δ considered in each case will be also mentioned for the CFL equation of state, so that, for example, CFL200 represents the CFL EOS with $\Delta = 200$. For the bag constant B we adopt the value $4B = 4.2 \times 10^{14} \text{ g/cm}^3$, while for the mass of the strange quark we take the value $m_s = 150 \text{ MeV}$.

The pressure-density relation is presented for the considered equations of state in Fig. 1.

In order to calculate the equilibrium configurations of the rotating neutron and quark

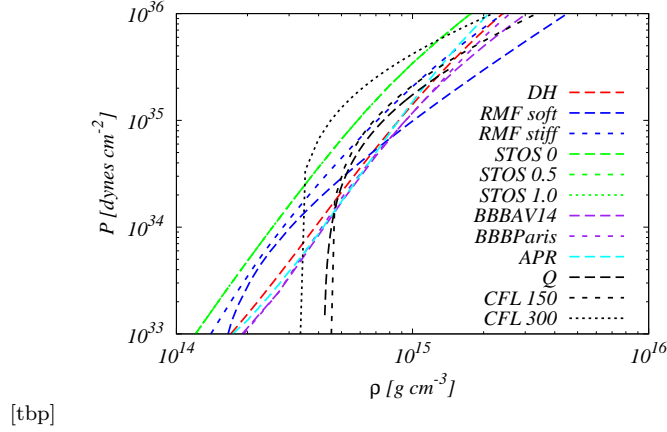


Figure 1. Pressure as a function of density (in a logarithmic scale) for the equations of state DH, RMF soft, RMF stiff, STOS 0, STOS 0.5, STOS 1, BBBAV14, BBBParis, APR, Q, CFL150, and CFL300, respectively.

stars with the EOS's presented here we use the RNS code, as introduced in Stergioulas & Friedman (1995), and discussed in details in Stergioulas (2003). This code was used for the study of different models of rotating neutron stars (Nozawa et al. 1998), and for the study of the rapidly rotating strange stars (Stergioulas et al. 1999). The metric outside the rotating compact general relativistic stars can be described, in quasi-isotropic coordinates, as

$$ds^2 = -e^{\gamma+\rho} dt^2 + e^{2\alpha} (d\bar{r}^2 + \bar{r}^2 d\theta^2) + e^{\gamma-\rho} \bar{r}^2 \sin^2 \theta (d\phi - \omega dt)^2, \quad (29)$$

where the metric potentials γ , ρ , α and the angular velocity of the stellar fluid relative to the local inertial frame ω are all functions of the quasi-isotropic radial coordinate \bar{r} and of the poloidal angle θ . The RNS code computes the metric functions in a quasi-spheroidal coordinate system and write them as functions of the compactified dimensionless distance $s = \bar{r} / (\bar{r} + \bar{r}_e)$, where \bar{r}_e is the equatorial radius of the star, and the cosine of the poloidal angle. The quasi-spheroidal radial coordinate is converted into curvature coordinate r according to the equation $r = \bar{r} \exp \{ [\gamma(\bar{r}, \theta) - \rho(\bar{r}, \theta)] / 2 \}$.

5 THE ISOTHERMAL THIN DISK

With the assumption that the surface of the thin accretion disk is in an isothermal state, (which is definitely a crude approximation), the effective temperature T_{eff} of the disk surface can be set to a constant over the entire disk. Following (Asano & Fukuyama 2001), we use a constant effective temperature measured at $3r_g$, $T_{eff} = T_{eff}(3r_g)$, with T_{eff} in the range of 10 to 20 MeV. In this case the radial dependence of the neutrino temperature T_0 is determined only by the gravitational redshift, and the Lorentz boost, as can be seen in Eq. (22). Since the neutrinosphere either does not exist (if the central body is not compact enough), or its

equatorial radius is smaller than the stellar radius, for the configurations of the neutron and quark star models presented here, the entire surface of the accretion disk can be considered as a neutrino source (Kovács et al. 2010).

As it has been showed before, if black holes spin up the energy deposition via the neutrino pair annihilation is increasing at the rotational axis of the black hole (Asano & Fukuyama 2001; Miller et al. 2003). This phenomenon is a consequence of the decreasing radius of the marginally stable orbit, i.e., of the increasing surface area of the accretion disk with the increasing spin. However, this enhancement is moderated by the redshift of the neutrinos emerging from the innermost region of the disk, which causes a smaller and smaller increment in the EDR as the spin parameter is approaching one. The Doppler shift due to the disk rotation has also to be taken into account when we calculate the net temperature effect on the axial distribution of the EDR.

If the central body is a neutron or quark star, then the situation is even more complicated. In many cases there is no marginally stable orbit outside the star and the inner edge of the accretion disk is located at the stellar surface. Then the proportionality between the area of the disk surface and the spin is no longer guaranteed, and it indeed breaks down at higher rotational frequencies for some physical configurations of stars, and for some EOS types where inner disk edge touches the stellar surface.

In Table 1 we present the relation between the spin parameter, the radius of the inner edge of the disk, and the enhancement in the EDR. Here we have integrated the EDR given by Eq. (23) over $r = 3 - 10r_g$ for each configuration, $\text{EDR} = \int_{3r_g}^{10r_g} (dE_0/dt)_{\theta=0} dr$, and we have computed $\Delta\text{EDR} = (\text{EDR} - \text{EDR}_s) / \text{EDR}_s$, where EDR_s is derived from the Schwarzschild geometry. The cutoff radius R_{out} of the accretion disk was set to $10r_g$. In the calculations we used the metric provided by the RNS code for the total mass $M = 1.8M_\odot$, and different angular velocities between $5 \times 10^2 \text{ s}^{-1}$ and $5 \times 10^3 \text{ s}^{-1}$. The tables containing the physical parameters of these stellar configurations can be found in Appendix C.

For the first four stellar models presented in Table 1, namely those with DH, APR, BBBAV14 and BBBParis type EOS's, the EDR is increasing as the disk surface is increasing (R_{in} is decreasing) with the increasing spin of the star. Since at the rotation frequency of $5 \times 10^3 \text{ s}^{-1}$ the value of the spin parameter is only about 0.3 – 0.35, the increase in the EDR as compared to the EDR obtained for a static star or black hole is only $\sim 7\%$. For a black hole spinning up to $a_* = 0.99$, this enhancement is already 30% (Asano & Fukuyama 2001)

We also present the axial distribution of the EDR for these stellar models in Fig. 2,

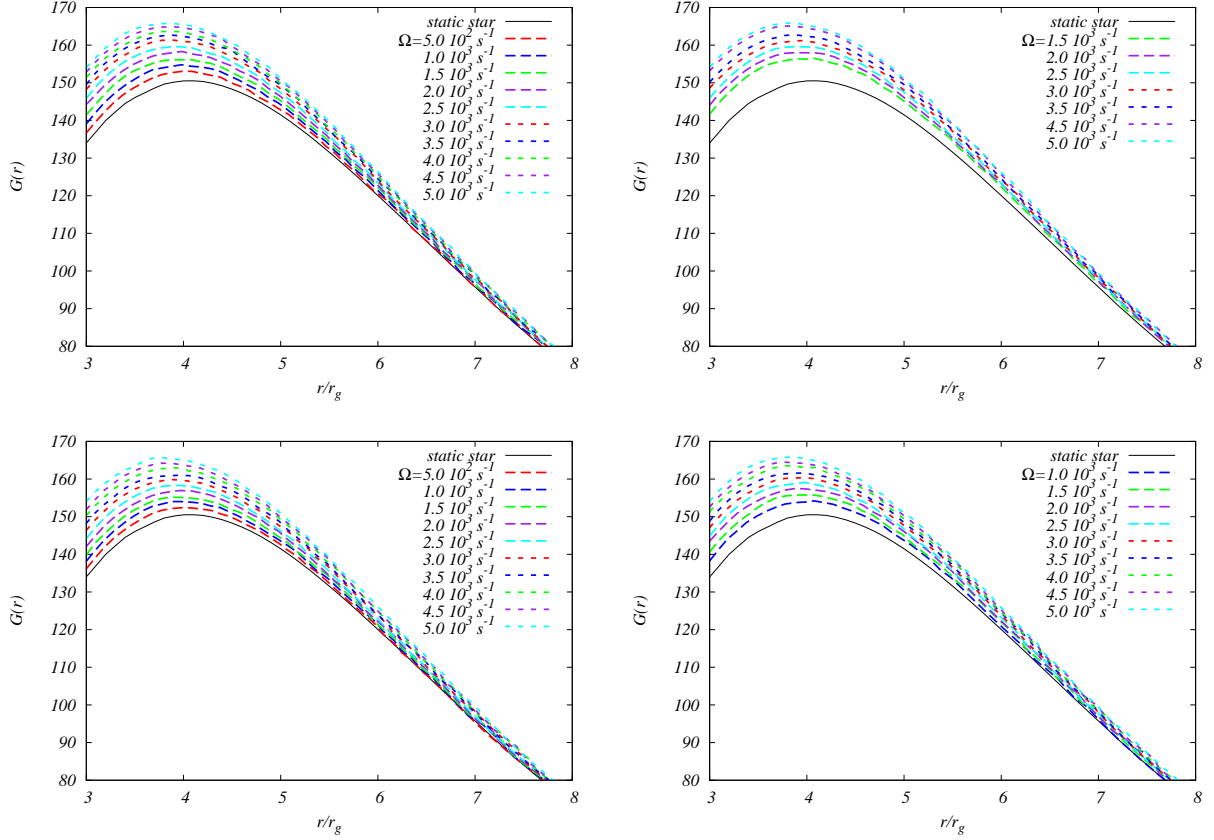


Figure 2. The axial profile of the EDR characterized by the dimensionless quantity $G(r)$ as a function of Ω for an isothermal accretion disk and neutron star models with DH (top left hand side), APR (top right hand side), BBBV14 (bottom left hand side) and BBBParis (bottom right hand side) type EOS. The total stellar mass is $1.8M_{\odot}$. For comparison we also plotted $G(r)$ for a static spacetime geometry (black solid curve).

where we have plotted the quantity $G(r)$, defined in Eq. (24), as a function of the curvature coordinate r . The graphs show that the proportionality between the maximum of the deposition rate and the spin parameter of the star is also preserved: the faster the neutron star rotates, the higher the maximal value of the EDR along the axis. Nevertheless, these maxima shift closer to the stellar surface for higher angular velocities, which involves the baryon contamination problem. Besides the uncertainties arisen from baryon contamination, one must be careful with the interpretation of these results, since the application of a formalism developed for black holes may produce considerable errors at higher values of Ω . As the error due to the separation of the geodesic equation is increasing with the higher rotational speed of the central object, the calculations produce less reliable results for high Ω . Hence it is not clear that the moderate increase in the EDR at higher angular frequencies is the result of the effect of the redshift of the neutrino/anti neutrino energy alone, or it is caused by the underestimation of the real values in the approximation. The latter must at

EOS	Ω [10^3s^{-1}]	0.5	1.0	1.5	2.0	2.5	3.0	3.5	4.0	4.5	5.0
DH	a_*	0.03	0.07	0.10	0.13	0.17	0.21	0.24	0.27	0.31	0.35
	R_{in}/r_g	2.94	2.89	2.85	2.79	2.75	2.70	2.67	2.63	2.60	2.56
	ΔEDR (isothermal) [%]	1.11	1.95	2.59	3.38	4.17	5.20	5.98	6.19	6.96	7.56
	ΔEDR ($T_{eff}(R)$) [%]	12.8	25.0	37.0	51.9	66.9	85.9	100.6	115.8	133.3	149.6
APR	a_*	-	-	0.10	0.14	0.17	0.20	0.24	0.27	0.31	0.35
	R_{in}/r_g	-	-	2.84	2.79	2.75	2.71	2.66	2.63	2.59	2.56
	ΔEDR (isothermal) [%]	-	-	1.51	3.35	4.16	5.00	5.82	6.44	6.70	7.59
	ΔEDR ($T_{eff}(R)$) [%]	-	-	36.5	53.1	66.6	83.3	102.0	115.7	134.6	149.1
BBBAV14	a_*	0.03	0.05	0.08	0.11	0.13	0.16	0.19	0.23	0.26	0.29
	R_{in}/r_g	2.95	2.91	2.88	2.83	2.79	2.75	2.71	2.66	2.62	2.58
	ΔEDR (isothermal) [%]	0.19	1.12	1.81	2.73	3.54	4.37	4.91	5.62	6.30	7.14
	ΔEDR ($T_{eff}(R)$) [%]	9.8	19.4	28.5	41.2	53.5	68.8	83.7	102.2	120.2	143.2
BBBParis	a_*	-	0.06	0.09	0.12	0.15	0.18	0.21	0.24	0.27	0.31
	R_{in}/r_g	-	2.90	2.86	2.81	2.77	2.73	2.69	2.64	2.61	2.57
	ΔEDR (isothermal) [%]	-	1.71	2.49	3.38	4.11	4.84	5.57	6.39	6.47	6.94
	ΔEDR ($T_{eff}(R)$) [%]	-	21.0	32.8	47.3	60.2	74.4	90.0	111.5	124.5	144.7
RMF stiff	a_*	0.05	0.09	0.14	0.20	0.25	0.30	0.36	0.43	0.51	0.63
	R_{in}/r_g	2.92	2.87	2.81	2.77	2.75	2.63	2.67	2.75	2.83	2.96
	ΔEDR (isothermal) [%]	1.65	2.62	3.65	4.37	4.88	6.03	5.72	4.50	3.29	2.09
	ΔEDR ($T_{eff}(R)$) [%]	16.8	32.0	48.0	62.4	70.0	114.6	96.8	68.7	40.8	6.5
STOS0	a_*	0.06	0.12	0.17	0.24	0.30	0.38	0.46	0.56	0.69	0.86
	R_{in}/r_g	2.92	2.87	2.88	2.90	2.96	3.00	3.10	3.21	3.43	3.84
	ΔEDR (isothermal) [%]	1.88	2.69	3.05	2.96	1.96	1.65	-0.41	-1.49	-6.08	-12.36
	ΔEDR ($T_{eff}(R)$) [%]	21.7	36.2	34.7	27.3	14.8	4.5	-15.0	-31.2	-56.6	-80.0
Q	a_*	-	-	0.11	0.15	0.19	0.23	0.28	0.32	0.37	0.41
	R_{in}/r_g	-	-	2.83	2.78	2.74	2.71	2.67	2.67	2.67	2.67
	ΔEDR (isothermal) [%]	-	-	2.99	4.01	4.54	5.11	5.48	5.82	5.92	6.37
	ΔEDR ($T_{eff}(R)$) [%]	-	-	40.2	55.8	70.5	84.1	96.3	101.6	102.5	100.2
CFL150	a_*	-	0.08	0.13	0.17	0.21	0.26	0.31	0.36	0.41	0.47
	R_{in}/r_g	-	2.88	2.82	2.77	2.73	2.71	2.69	2.70	2.73	2.79
	ΔEDR (isothermal) [%]	-	2.15	3.07	4.10	4.59	5.06	5.30	5.47	5.20	5.06
	ΔEDR ($T_{eff}(R)$) [%]	-	28.7	44.1	60.3	72.5	82.3	88.6	88.3	78.0	59.0

Table 1. The spin parameter a_* of the star, the inner edge R_{in} of the accretion disk, and the variation in the EDR integrated over the rotational axis for neutron and quark star models, with a total mass of $1.8M_\odot$ and angular velocities from $5 \times 10^2 \text{s}^{-1}$ to $5 \times 10^3 \text{s}^{-1}$. Here $\Delta \text{EDR} = (\text{EDR} - \text{EDR}_s)/\text{EDR}_s$ and EDR_s is derived for the static case ($\Omega = 0$). The variation in EDR is calculated for both isothermal disks ($T_{eff}=\text{const}$) and disks with the temperature profile $T_{eff}(R) = T_{eff} \times 3r_g/R$.

least not dominate over the real physical effects, as far as we consider configurations with lower values of the spin parameter (see Appendix A).

From the off-axis calculations of the spatial distribution of the EDR in the vicinity of Kerr black holes we already know that the increase in the rotational speed of the black hole enhances the energy deposition along both the equatorial plane, and the axis of rotation (Miller et al. 2003). This may indicate that the behavior presented in Fig. 2 is in accordance with the previous results on the EDR distribution along the equatorial plane for the same family of stellar EOSs (Kovács et al. 2010). It was shown that for the APR type EOS the maximum of the energy deposition from $\nu\bar{\nu}$ pair annihilation is increasing along the surface of the thin accretion disk as the star spins up. The other types of EOS shown in Fig. 2

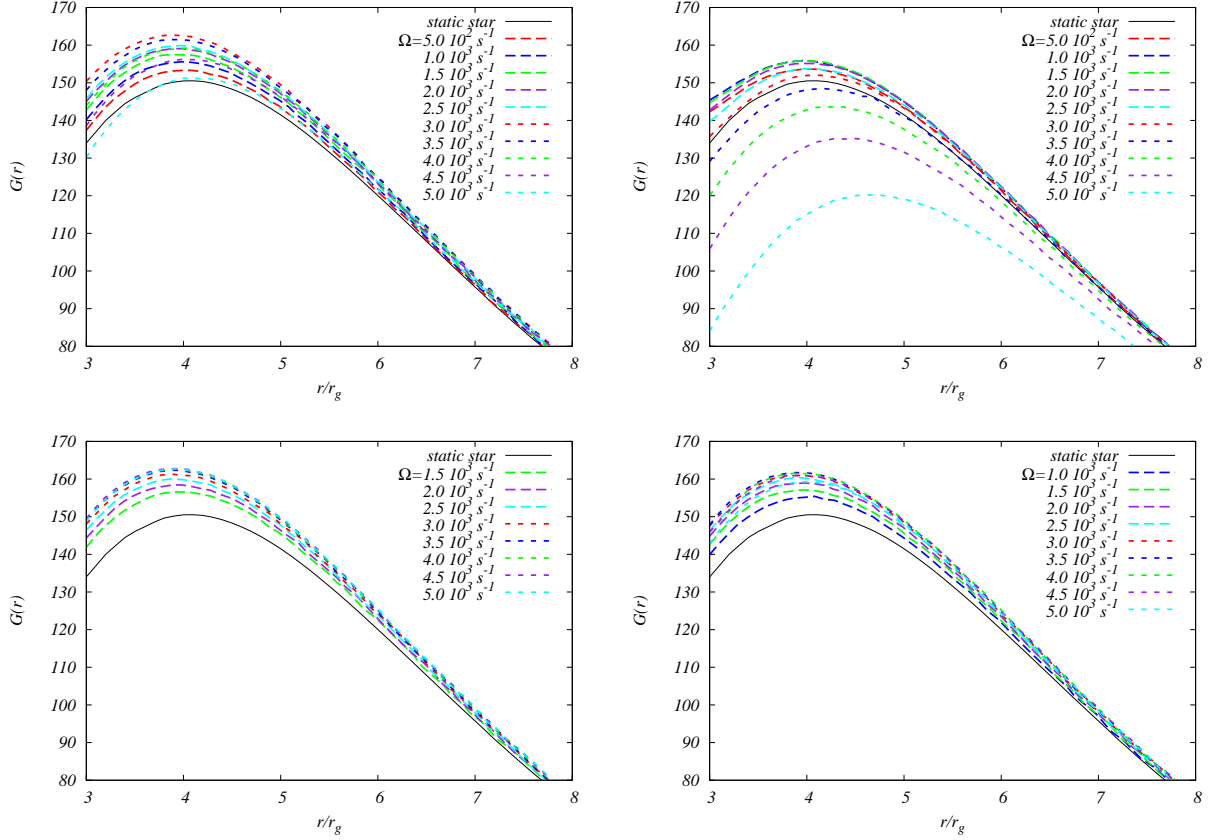


Figure 3. The axial profile of EDR characterized by the dimensionless quantity $G(r)$ as a function of Ω for an isothermal disk and neutron star models with RMF stiff (top left hand side) and STOS0 (top right hand side) type EOSs, and for quark stars with Q (bottom left hand side) and CFL 150 (bottom right hand side) type EOSs.

exhibit similar behaviors. Therefore we can conclude that they follow the pattern found in the case of Kerr black holes.

The neutron star models with RMF stiff and STOS0 type EOS, together with the Q and CFL 150 type quark stars do not produce a simple relation between the spin and the EDR, as shown in the bottom four lines of Table 1. In Fig. 3 we also present the dependence of the EDR on Ω for these models. In the case of the neutron stars with RMF stiff and STOS0 type EOSs there is some enhancement in the EDR for rotational velocities increasing up to $\sim 3 \times 10^3 \text{ s}^{-1}$ (RMF stiff) and $\sim 1.5 \times 10^3 \text{ s}^{-1}$ (STOS0), but at higher values of Ω the maxima of the ERD starts to decrease. As the star rotates faster its surface reaches higher equatorial orbits, and reduces the surface area of the accretion disk by pushing the inner edge of the disk to higher radii. At rotational frequencies approaching $5 \times 10^3 \text{ s}^{-1}$ the amount of the energy deposition for the stellar model with RMF stiff type EOS reduces to the one derived in the static case. Since the stellar radius is already much greater than $r_{ms} = 3r_g$ of

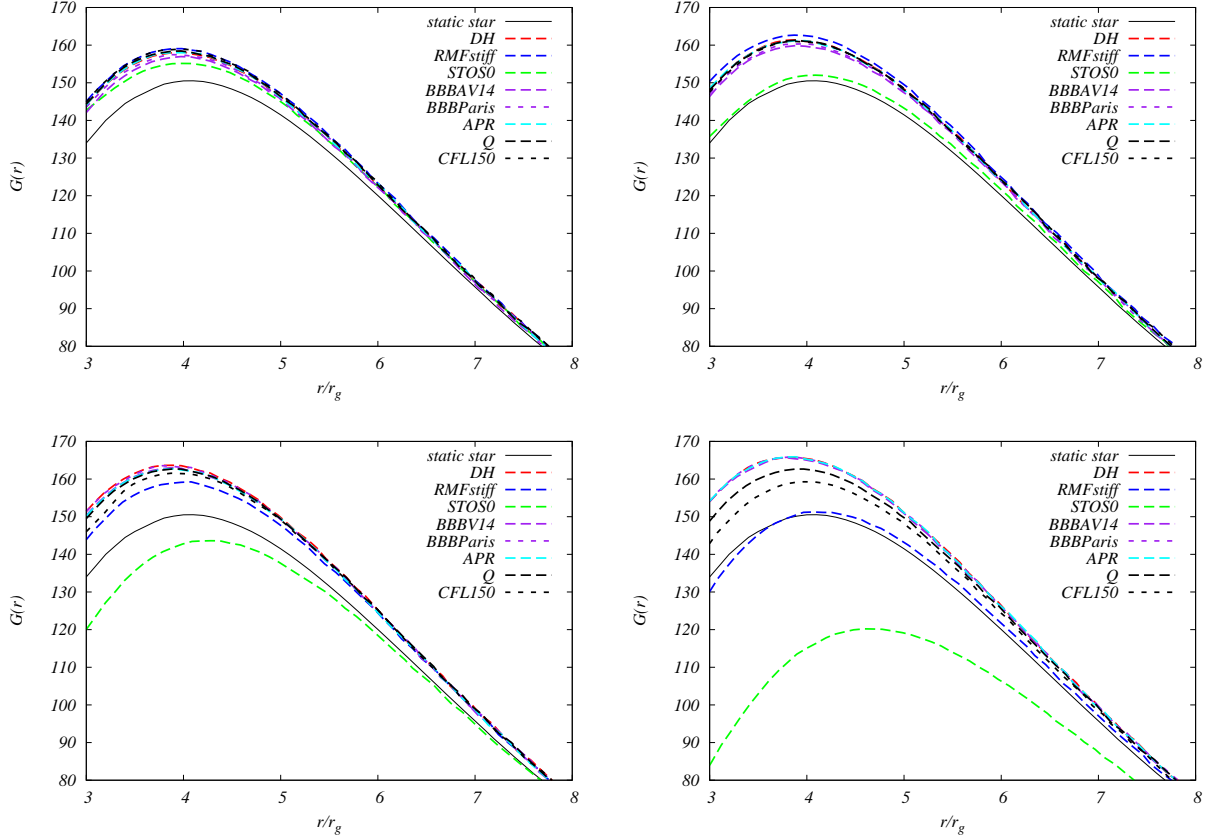


Figure 4. The axial profile of the EDR, characterized by the dimensionless quantities $G(r)$ for an isothermal disk, and different neutron and quark star models with the total mass $M = 1.8M_\odot$ and rotational velocities $\Omega = 2 \times 10^3 \text{ s}^{-1}$ (top left hand side panel), $3 \times 10^3 \text{ s}^{-1}$ (top right hand side panel), $4 \times 10^3 \text{ s}^{-1}$ (bottom left hand side panel) and $5 \times 10^3 \text{ s}^{-1}$ (bottom right hand side panel).

the static case, we obtain even smaller values of the EDR for the STOS0 model than those derived for a static star (see the negative values in Table 1).

The quark star models with Q and CFL150 type EOS do not deviate so drastically from the spin-EDR relation characterizing the first family of EOSs and the black holes. In Fig. 3 we can see that the maximum of the EDR has an increase, turns over, and then decreases with increasing spin parameter. However, its reduction after the turn over is minimal, and it might be a result of the combination of several physical effects, such as the variation of the disk surface area, the redshift and the Lorentz boost, together with the artifacts caused by the break-down of our approximation for higher values of the spin parameter. The total EDR integrated along the rotational axis remains increasing for the Q type EOS, but the differences are small, and may be dominated by the uncertainties for fast stellar rotation. These results are still in good agreement with the fact that the amount of energy liberated in the $\nu\bar{\nu}$ pair annihilation along the equatorial plane is proportional to the angular velocity of

the quark star with Q type EOS, as far as we compare the configurations for $\Omega = 3 \times 10^3 \text{ s}^{-1}$ and $5 \times 10^3 \text{ s}^{-1}$ with each other (Kovács et al. 2010).

In Fig. 4 we also compare the EDR distributions calculated along the rotational axis for different EOS types at constant angular frequencies ranging from $\Omega = 2 \times 10^3 \text{ s}^{-1}$ to $5 \times 10^3 \text{ s}^{-1}$, respectively. The plots show that the quark stars and the neutron stars with RMF stiff type EOS produce the highest values of the EDR at low rotational frequencies, although the differences are not considerable. This relation is similar to the one derived in the equatorial plane, where the EDR is higher for quark stars than for neutron stars, apart from those with RMF stiff and STOS0 EOS type (Kovács et al. 2010). The only difference is the behavior of the STOS0 model, which has somewhat lower values in the EDR along the rotational axis than other neutron star models do. However, the EDR values in the equatorial plane were derived at $\Omega = 5 \times 10^3 \text{ s}^{-1}$ in (Kovács et al. 2010), and we should compare them with the plots displaying configurations with high rotational velocities.

The comparison shows that quark stars and neutron stars with RMF stiff and STOS0 type EOS generate less energy along the rotational axis from the neutrino-anti neutrino annihilation than the neutron stars with other EOS types do at $\Omega = 5 \times 10^3 \text{ s}^{-1}$, as opposed to the relations between the values of EDR calculated in the equatorial plane. In fact, there is no discrepancy between the two results, as the EDR at a given point R in the equatorial plane is calculated by integrating the angular part of Eq. (14) between R and R_{out} (Salmonson & Wilson 1999), whereas the calculation of the EDR at a point r on the rotational axis always involves the integral of Eq. (14) over the entire accretion disk (Asano & Fukuyama 2001). As a result, the first method provides \dot{q} for any value $R > R_{in}$, which does not depend on R_{in} (the latter one is only a lower boundary of the domain of \dot{q}), whereas the EDR derived by the second method always depends on R_{in} , i.e, the area of the disk surface.

Nevertheless, the results presented here are already uncertain in the regime of high angular frequencies, and the EDR along the rotational axis should already be calculated for rapidly rotating stars by applying the fully 3D techniques of off-axis calculations.

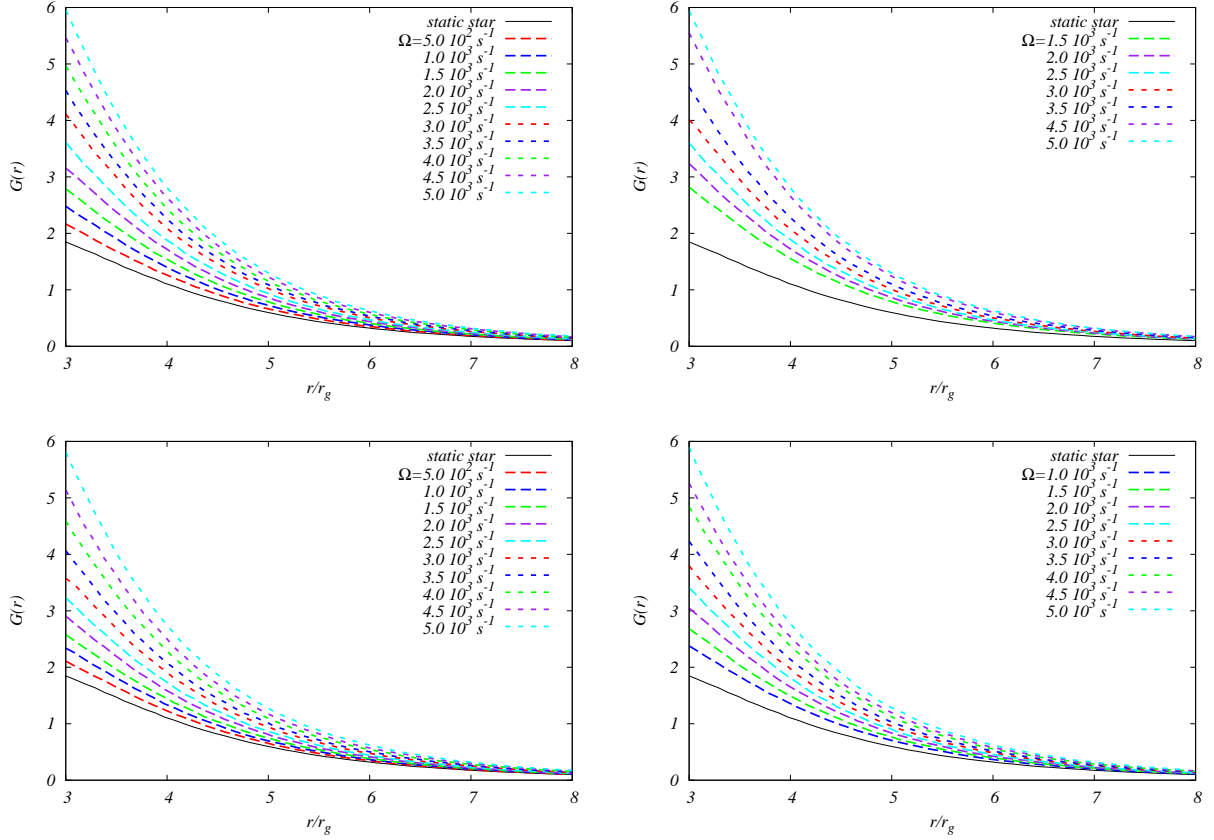


Figure 5. The axial profile of the EDR characterized by the dimensionless quantity $G(r)$ for $T_{eff} \propto R^{-1}$ and different angular velocities of the neutron star models with DH (top left hand side), APR (top right hand side), BBBV14 (bottom left hand side) and BBBParis (bottom right hand side) type EOSs. (The total mass of the central object is $1.8M_{\odot}$.) For comparison we have also plotted $G(r)$ for a static spacetime geometry (black solid curve).

6 THIN DISK WITH RADIATION IN THERMODYNAMICAL EQUILIBRIUM

In this Section we use for the calculation of the EDR along the rotational axis for various rotating compact objects a more realistic model of the thermal distribution of the neutrino flux emerging from the thin accretion disk. This model is based on the thermodynamical equilibrium approximation of the state of the accretion disk, where the temperature gradient is given by a profile inversely proportional to the radius. Following Asano & Fukuyama (2001), we replace the constant temperature profile $T_{eff} = T_{eff}(3r_g)$ with $T_{eff}(R) = T_{eff}(3r_g) \times 3r_g/R$, and we recalculate the EDR along the rotational axis for all the constant disk temperature configurations considered before.

In Figs. 5 and 6 we present the axial distribution of the EDR derived for the accretion disk with temperature gradient. If we compare the results with those obtained in the isothermal case for the same $T_{eff}(3r_g)$, we see that the EDR is reduced by a factor of 100 at low rotational frequencies of the central body. Even for the highest values of Ω , the EDR in the

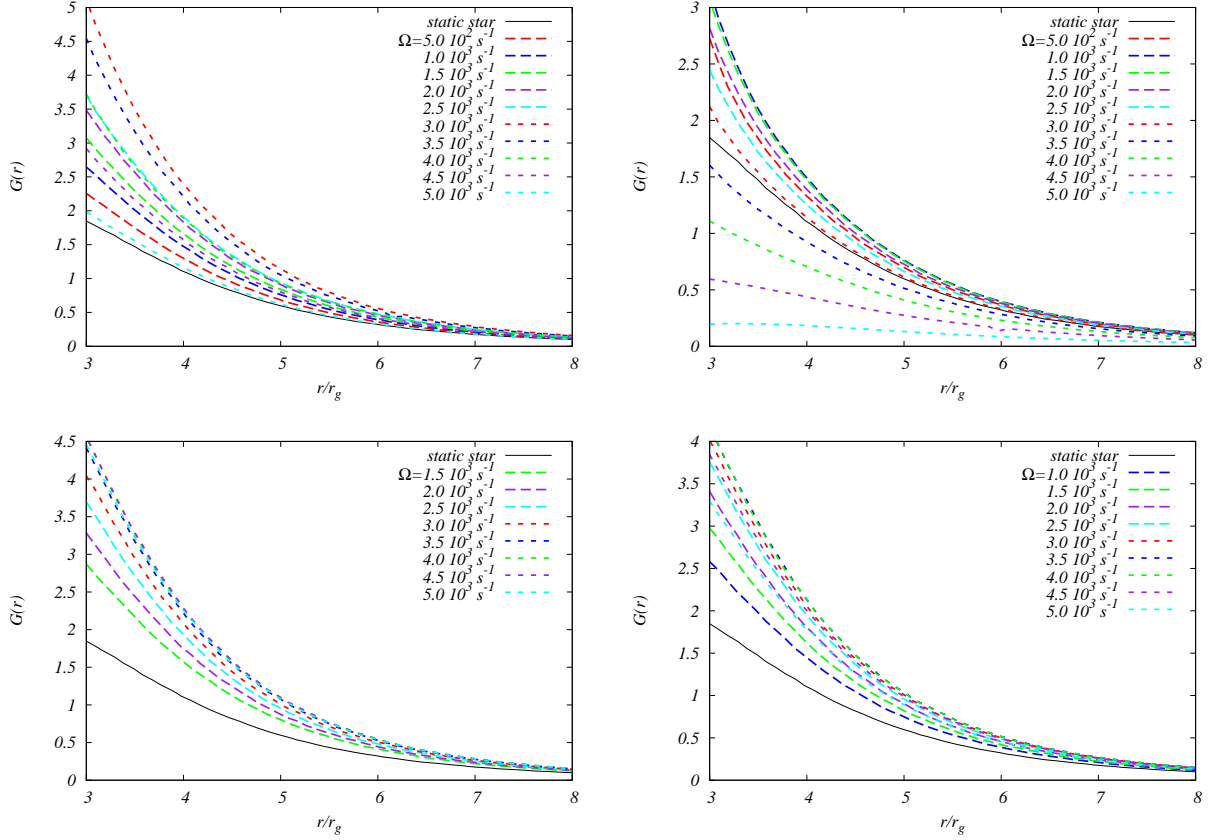


Figure 6. The axial profile of the EDR characterized by the dimensionless quantity $G(r)$ for $T_{eff} \propto R^{-1}$, and different angular velocities of the neutron star models with RMF stiff (top left hand side) and STOS0 (top right hand side) type EOSs, and for quark stars with Q (bottom left hand side) and CFL 150 (bottom right hand side) type EOSs.

isothermal case is about 25 times higher than the one calculated with temperature gradient. Only the dynamical range of the EDR became wider for the first group of EOS in Fig. 5: in the isothermal case its values at $r \sim 3r_g$ have a $\sim 10\%$ increase for $\Omega = 5 \times 10^3 \text{ s}^{-1}$, as compared with those for $\Omega = 5 \times 10^2 \text{ s}^{-1}$. The difference increases to a factor of 3 for the disk with the temperature gradient. Table 1 also contains the differences of the total EDR integrated over $r = 3r_g - 10r_g$ for these configurations for a disk with the R -dependent temperature profile. The differences in the total EDR compared with the static case are from $\sim 10\%$ to $\sim 150\%$, which span a much wider range than those for the isothermal disk do, between ~ 1 and $\sim 7\%$. Although in the models with a disk temperature gradient the efficiency of the energy deposition compared with the static case increases in a much higher rate with increasing Ω , the comparison of Figs. 2 and 5 shows that even at high rotational velocities the EDR is much smaller for $T_{eff} \propto R^{-1}$ than the one calculated for isothermal disks. The plots also demonstrate that the EDR decreases more rapidly with r for the latter model than it does for isothermal disks, especially at higher angular velocities. This means

that the axial distribution of the EDR is more concentrated to the region close to the star, and the energy is produced here mainly by the neutrinos and anti - neutrinos emitted from the innermost region of the disk. For the temperature profile $T_{eff} \propto R^{-1}$, this region is hot, but the neutrinos leaving the rapidly rotating disk surface suffer a large Doppler shift, which, together with the large gravitational redshift, prevents them from depositing much energy at higher radii.

For the second group of the EOS types shown in Fig. 6, the EDR still preserves its non-linear dependence on the rotational velocity of the central body. Over $\Omega = 3 \times 10^3 \text{ s}^{-1}$ for the RMF stiff model and over 10^3 s^{-1} for the STOS0 EOS type their relation is inverted, and the EDR is approaching to, or even takes smaller values, than the one obtained in the static configuration. This trend is also present in the differences of the total EDR integrated along the axis, as can be seen in Table 1, where ΔEDR has a considerable reduction at higher values of Ω , as compared with its maxima.

The quark stars follow the similar trend, but with moderate deviations, as in the isothermal case. For higher rotational speeds in Table 1 the proportionality between the spin and the EDR is inverted, and we obtain a slight decrease in the total EDR as compared with the cases of slower rotation at $3.5 - 4 \times 10^3 \text{ s}^{-1}$.

In Fig. 7 we present $G(r)$ for accretion disks with a $T_{eff} \propto R^{-1}$ temperature profiles, rotating around stars with different EOSs types, but with fixed values Ω . These plots also show the same trends as those found in the case of the isothermal disk: at lower rotational frequencies the EDR is somewhat higher for the quark stars than the one derived for neutron stars - apart from the stellar model with RMF stiff type EOS - but with increasing Ω its value for the Q and the CFL150 type EOS drops below those of the stellar models with DH, APR, BBBAV14, and BBBParis EOSs, respectively. The only neutron stars producing less EDR at higher frequencies than the one obtained for the quark stars are the models with RMF stiff and STOS0 type EOS.

7 DISCUSSIONS AND FINAL REMARKS

In the present paper we have considered the energy deposition rate from the neutrino-antineutrino annihilation process on the rotation axis of rotating neutron and quark stars. The energy deposition rate has been obtained numerically for several equations of state of the neutron matter, and for two types of quark stars, respectively. All the general relativistic

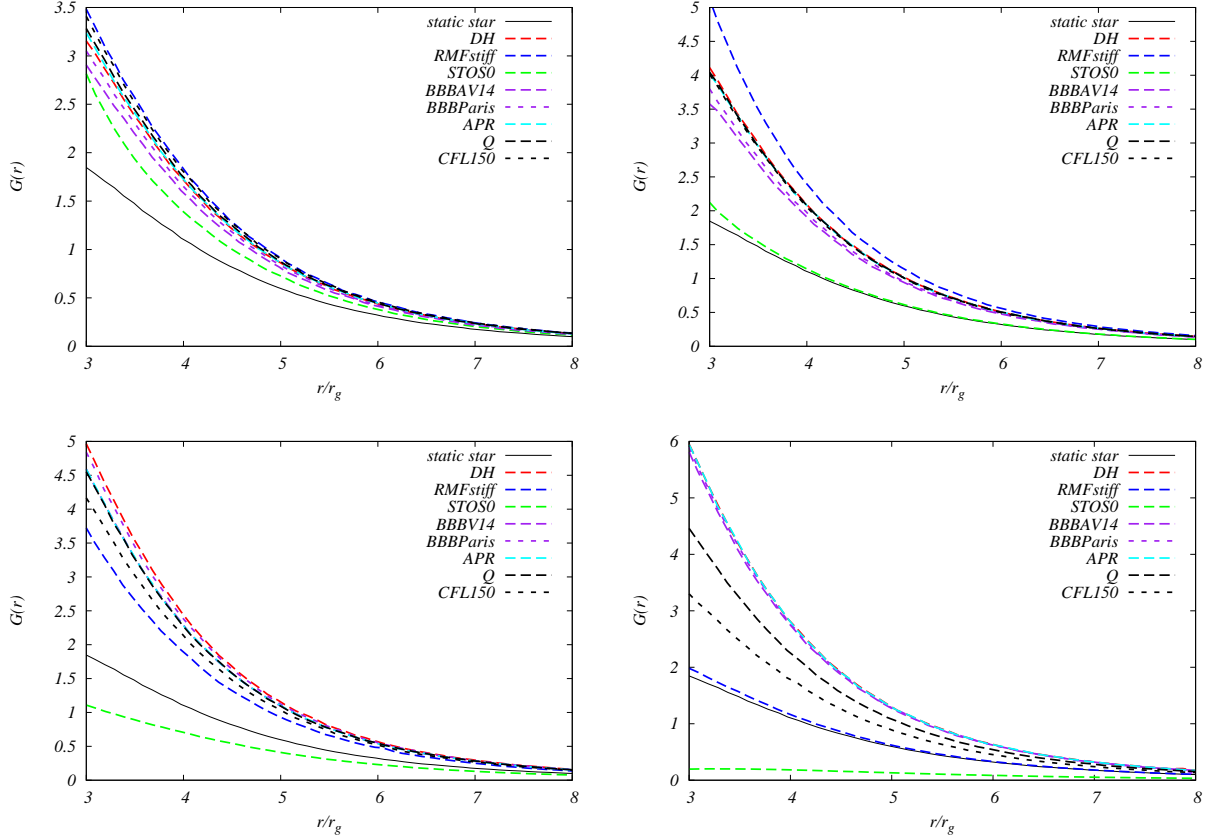


Figure 7. The axial profiles of the EDR characterized by the dimensionless quantities $G(r)$ for an isothermal disk, and different neutron and quark star models, with the total mass of the central object $M = 1.8M_{\odot}$, and rotational velocities $\Omega = 2 \times 10^3 \text{ s}^{-1}$ (top left hand side panel), $3 \times 10^3 \text{ s}^{-1}$ (top right hand side panel), $4 \times 10^3 \text{ s}^{-1}$ (bottom left hand side panel) and $5 \times 10^3 \text{ s}^{-1}$ (bottom right hand side panel).

correction factors, related to this process, can be obtained from the metric of the central compact object. In the present paper we have neglected the possible effects of the stellar magnetic field on the external geometry of the spacetime around the compact general relativistic effects, as well as on the motion of the neutrinos. Generally, we assume that the magnetic energy of the disk, $B^2/8\pi$ is much smaller than the $\rho V_K^2/2$, the kinetic energy density of the disk, $B^2/8\pi \ll \rho V_K^2/2$, where V_K is the Keplerian velocity. Hence we neglect the possible influence of the magnetic field on the temperature profile of the disk. Due to the differences in the space-time structure, the quark stars present some important differences with respect to the energy deposition rate, as compared to the neutron stars. As a general result we have found that there is a general correlation between the energy deposition rate and the spin parameter of the star. There is also a strong dependence between the temperature profile of the disk and the EDR, and at high rotational velocities the EDR is much smaller for the model with $T_{eff} \propto R^{-1}$ than the one calculated for the constant temperature (isothermal) disks. Our study is based on the main assumption of the separability of the

geodesic equations of motion for the neutrinos. Even that from a purely theoretical point of view the geodesic and the Hamilton-Jacobi equations cannot be separated, from a practical-computational point of view we have found that such a procedure can work, at least for low angular speeds, with a good precision, with the error introduced by this approximation not exceeding 1%.

In order to compare the properties of the quark and neutron stars we have chosen a common mass value $M = 1.8M_{\odot}$. Generally, quark stars may have masses greater than $1.8M_{\odot}$. However, for some equations of state of the neutron matter the maximum allowable mass could be smaller than the maximum mass of quark stars. Therefore we have chosen this particular value of the stellar mass in order to be able to compare sequences of quark stars and neutron stars for a large number of equations of state.

A possible astrophysical application of our results could be in the explanation of the physical processes that lead to the formation of the Gamma-Ray Bursts (GRBs). The so-called fireball model can basically explain the observational facts well, and thus it is strongly favored, and widely accepted today (for recent reviews on GRBs see Mészáros (2006) and Zhang (2007), respectively). Newborn neutron stars, surrounded by hyper-accreting and neutrino-cooled disks may exist in some gamma-ray bursts and/or supernovae. As compared with the black hole disk, the neutrino annihilation luminosity above the neutron star disk is higher (Zhang & Dai 2009). Although a heavily mass-loaded outflow from the neutron star surface at early times of neutron star formation prevents the outflow material from being accelerated to a high bulk Lorentz factor, if the disk accretion rate and the neutrino emission luminosity from the surface boundary layer are sufficiently high, an energetic ultra-relativistic jet via neutrino annihilation can be produced above the stellar polar region at late times. The energy deposition along the rotation axis will form a narrow cone jet, which encounters much less material, and hence it can maintain a large Lorentz factor.

The neutrino emission rate is also strongly dependent on the temperature. In the standard models of GRBs it is assumed that the central object is surrounded by a degenerate accretion disk, which allows super-Eddington accretion rates, of the order of one solar mass per second (Zhang 2007). If the central compact object is a neutron or a quark star, such super-Eddington accretion rates can maintain the compact object at very high temperatures, and thus allowing very high neutrino luminosities, as well as a high rate of electron-positron pair production. The neutrino temperature can be estimated by assuming that the accretion power $\eta\dot{M}c^2$, where η is the efficiency of the energy conversion and \dot{M} is

the accretion rate, is equal to the radiation power $4\pi R^2 \sigma T_\nu^4$, which gives the temperature as $T_\nu = (\eta \dot{M} c^2 / 4\pi R^2 \sigma)^{1/4}$. By taking $\eta = 0.1$, $R = 10^6$ cm, and an accretion rate of $\dot{M} = 1M_\odot/10$ s, we obtain $T_\nu = 7.14 \times 10^{10}$ K, a temperature which is of the order of MeV. Therefore, if the accretion disk is fed at a high rate, like, for example, by the fallback material after a supernova explosion, a high neutrino-antineutrino emission rate can be maintained, and this could explain some of the basic properties of the GRB phenomenon.

The neutrino annihilation and the electron-positron pair production also plays an essential role in the astrophysical processes associated with the phase transitions that could take place inside neutron stars. For example, the sudden phase transition from normal nuclear matter to a mixed phase of quark and nuclear matter induces temperature and density oscillations at the neutrinosphere. Consequently, pulsating neutrino/antineutrino and leptonic pair fluxes will be emitted (Cheng et al. 2009). During this stage several mass ejecta can be ejected from the stellar surface by the neutrinos and antineutrinos. These ejecta can be further accelerated to relativistic speeds by the electron/positron pairs, created by the neutrino and antineutrino annihilation outside the stellar surface. In order to produce the Gamma-Ray Bursts, a high neutrino emission rate is necessary. On the other hand, it is important to note that electron-positron pairs can deposit energy much more efficiently than the neutrinos, and the dominant energy deposition process is the neutrino-antineutrino annihilation process (Cheng et al. 2009). In fact most pairs are created outside the star. A large fraction of the neutrino energy, will be absorbed by the matter very near the stellar surface. When this amount of energy exceeds the gravitational binding energy, some mass near the stellar surface will be ejected, and this mass will be further accelerated by absorbing pairs created from the neutrino and antineutrino annihilation processes outside the star. This process may be a possible mechanism for short Gamma-Ray Bursts (Cheng et al. 2009).

ACKNOWLEDGMENTS

K. S. C. is supported by the GRF grant number HKU 7011/09P of the government of the Hong Kong SAR. The work of T. H. is supported by the GRF grant number 702507P of the Government of the Hong Kong SAR. Z.K. is indebted to Katsukai Asano and Gabe Perez-Giz for valuable discussions.

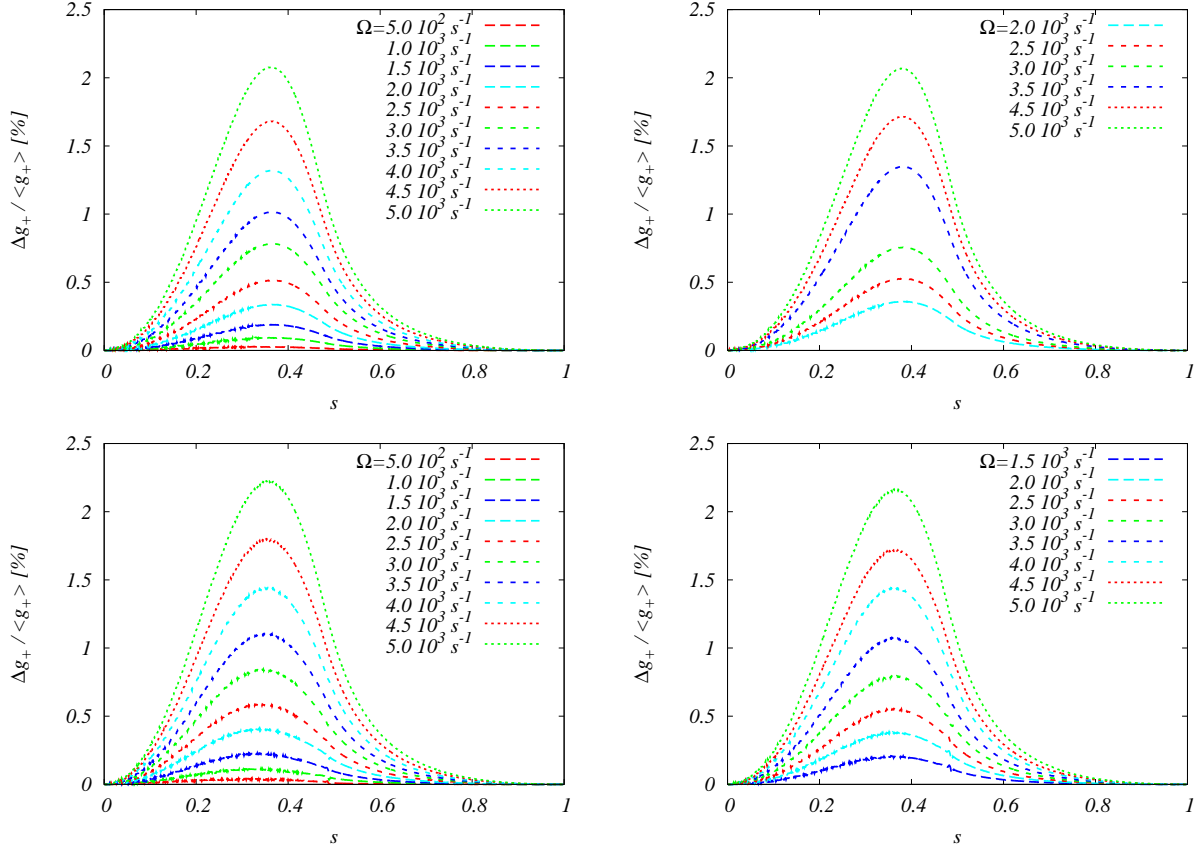


Figure A1. The $\Delta g_+ / \langle g_+ \rangle$ vs. s relation for neutron star models with various EOS types, such as DH, shown in Table C1 (top left hand side plot), APR, shown in Table C2 (top right hand side plot), BBBAV14, shown in Table C3 (bottom left hand side plot) and BBBParis shown in Table C4 (bottom right hand side plot).

APPENDIX A: THE SEPARABILITY OF THE GEODESIC EQUATION

The condition for the separability of the geodesic equation Eq. (2) for $L = 0$ is that the functions f and g_+ , given by Eqs. (3) and (8), respectively, must depend only on the radial coordinate r . This condition does not hold for general stationary and axially symmetric spacetimes, since the metric components are also functions of the polar angle. Now we examine if we can use the approximation of neglecting the angular dependence of the functions f and g_+ for the spacetime geometry of the neutron and quark stars which are considered in the present paper. If we insert the components $g_{\alpha\beta}$ of the metric (29), derived by the RNS code for these types of stars into Eqs. (3) and (8), we obtain $f(\bar{r}) = \bar{r}^2$, and an expression for g_+ which still depends on both \bar{r} and θ . Since f is the square of the radial coordinate only, the question is the angular dependence of g_+ . We consider the quantity $\Delta g_+ / \langle g_+ \rangle$ as a function of the dimensionless radial coordinate $s = \bar{r} / (\bar{r} + \bar{r}_e)$ (compactified in the domain $[0,1]$) and angle variable $\mu = \cos \theta$. Here Δg_+ is the maximal difference in the values of g_+ , and $\langle g_+ \rangle$ is the average of g_+ for a given s over the entire domain $[0,1]$ of μ . If g_+ has

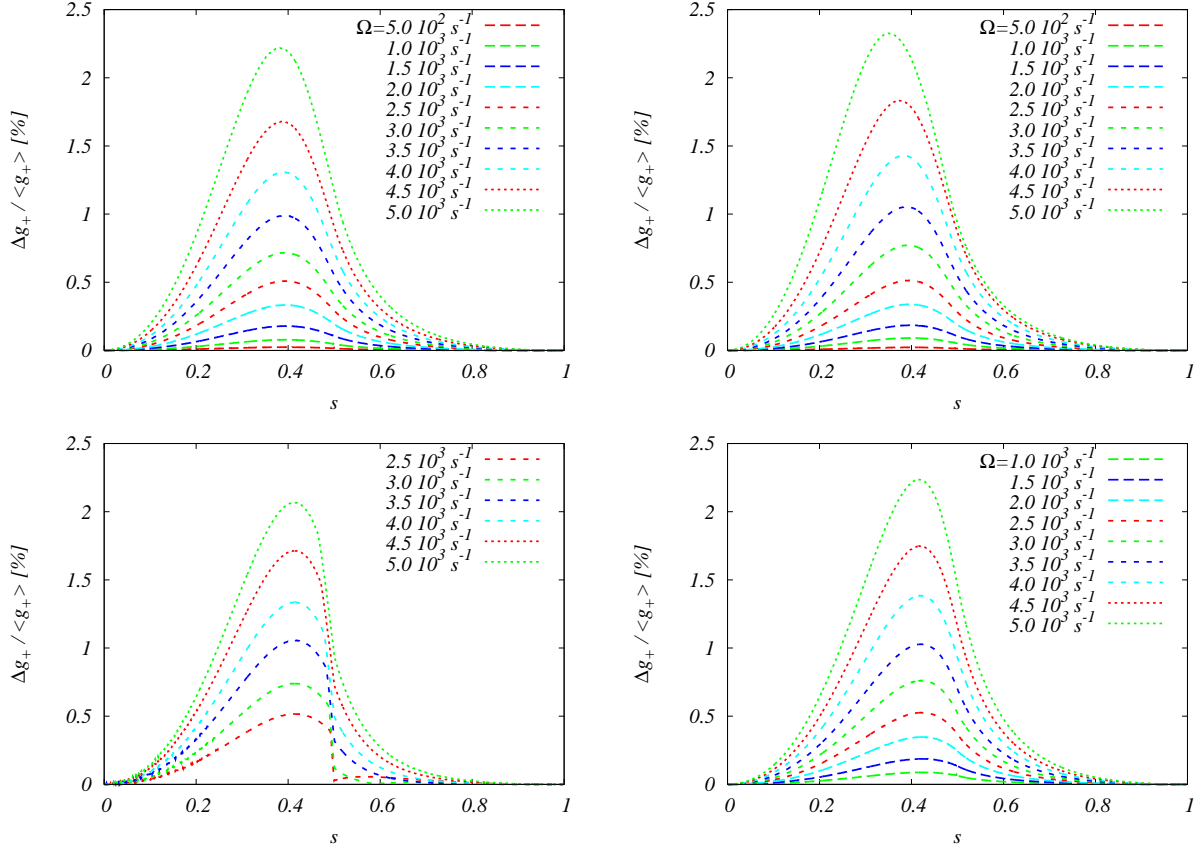


Figure A2. The $\Delta g_+ / \langle g_+ \rangle$ vs. s relation for neutron and quark star models with various EOS types, such as RMF stiff, shown in Table C5 (top left hand side plot), STOS0, shown in Table C6 (top right hand side plot), Q, shown in Table C7 (bottom left hand side plot) and CFL150 shown in Table C8 (bottom right hand side plot).

no angular dependence, as in the case of the Kerr spacetime (in both Boyer-Lyndquist and quasi-isotropic coordinates), this quantity is just zero. Its deviation from zero characterizes the limits of the validity of our approximation. In Figs. A1 and A2 we plot this function versus the coordinate s for all the stellar models we have studied in this work.

By definition of the coordinate s , the stellar surface in the equatorial plane is located at $s = 0.5$ and still remains close to this value at higher latitude. Therefore, the half of the right hand side of each plot represents the region of the spacetime outside the star. The accretion disk is rotating in this region, and the null geodesics emanating from the disk and intersecting the rotational axis at radii higher than $3r_g$ mostly remain located in this region as well. The trajectories originating at the inner disk edge might run inside the star, but we consider only those particles which hit the axis at $3r_g$ or higher radii. However, this minimal value is high enough to keep these trajectories close to the stellar surface ($s \lesssim 0.5$). In the case of the low mass stellar models with $M = 1.8M_\odot$, $\Delta g_+ / \langle g_+ \rangle$ is under 0.5% for $\Omega = 2 \times 10^3 \text{ s}^{-1}$, while it is more the 1% for angular velocities higher than $4 \times 10^3 \text{ s}^{-1}$. Then

on the one hand we do not expect that the separation of Eq. (2) causes large errors in the computation of scalar product $\mathbf{p} \cdot \mathbf{p}$ for slowly rotating objects, with $\Omega \sim 2 \times 10^3 \text{s}^{-1}$. On the other hand, the results derived for $\Omega \gtrsim 4 \times 10^3 \text{s}^{-1}$ have an increasing uncertainty as the error propagation grows due to the non-separability of Eq. (2), containing $g_+(r, \theta)$, which does depend on θ .

APPENDIX B: THE RAY TRACING ALGORITHM

The Hamilton-Jacobi equation (2) can be written as

$$\frac{g_{\theta\theta}}{g_{rr}} \dot{r}^2 + \dot{\theta}^2 = g_{\theta\theta} V(\omega_0, L), \quad (\text{B1})$$

where the effective potential is given by

$$V(\omega_0, L) = \frac{g_{\phi\phi}(\omega_0/c)^2 + 2g_{t\phi}(\omega_0/c)L + g_{tt}\tilde{L}^2}{g_{t\phi}^2 - g_{tt}g_{\phi\phi}}.$$

This is generally not a separable differential equation for the coordinates r and θ . For given initial values of the coordinates at some time $\tau = \tau_0$, and for fixed constants of motion ω_0 and L , we can, at least numerically, integrate this equation, to obtain the world-line projected onto the $r - \theta$ plane of a particle moving in the effective potential V . The only technical difficulty in the integration may stem from the non-separability of Eq. (B1). However, this can be easily circumvented by introducing the momenta p_r and p_θ and by replacing Eq. (B1) with their canonical equations of motion (Perez-Giz & Levin 2009). Then the complete set of the evolution equations is

$$\dot{r} = \frac{p_r}{g_{rr}}, \quad (\text{B2})$$

$$\dot{\theta} = \frac{p_\theta}{g_{\theta\theta}}, \quad (\text{B3})$$

$$\dot{p}_r = \frac{1}{2} \left(\frac{g_{rr,r}}{g_{rr}^2} p_r^2 + \frac{g_{\theta\theta,r}}{g_{\theta\theta}^2} p_\theta^2 - V_{,r} \right), \quad (\text{B4})$$

$$\dot{p}_\theta = \frac{1}{2} \left(\frac{g_{rr,\theta}}{g_{rr}^2} p_r^2 + \frac{g_{\theta\theta,\theta}}{g_{\theta\theta}^2} p_\theta^2 - V_{,\theta} \right), \quad (\text{B5})$$

together with the decoupled geodesic equation for the coordinates t and ϕ . This is a system of ordinary differential equations, with the unknown functions $r(\tau)$, $\theta(\tau)$, $p_r(\tau)$ and $p_\theta(\tau)$, respectively. The parameters appearing in the system are the constants of motion $p_t = -\omega_0/c$ and $p_\phi = L$. If the initial values of the unknown functions and of the parameters are given, so that the mass-shell condition $\mathbf{p} \cdot \mathbf{p} = 0$ holds (a constraint imposed on the initial data), then the system (B2)-(B5) can be integrated numerically. We have applied the fourth order

Runge-Kutta method for this system of differential equations to implement a ray tracing algorithm by reversing the proper time evolution.

In order to input the metric components $g_{\alpha\beta}$ in these equations, we have used numerical tables of the metric functions α , γ , ρ and ω , generated by the code RNS with a high resolution mesh (1001×501) of the compactified quasi-isotropic radial coordinate $s = \bar{r}/(\bar{r} + \bar{r}_e)$, and the angular coordinate $\mu = \cos \theta$. Since the numerical scheme of the ray tracing code needs to evaluate the functions $g_{\alpha\beta} = g_{\alpha\beta}(\alpha(s, \mu), \gamma(s, \mu), \rho(s, \mu), \omega(s, \mu))$, defined over the 2-dimensional grid (s, μ) at any arbitrary point (\bar{r}, θ) , we applied bi-cubic interpolation between the discrete points of the numerical tables. The derivatives with respect to r and θ (or \bar{r} and θ) in the evolution equations were replaced by finite differences, with a fine mesh, which we could calculate in any point from the quasi continuous interpolated function values. For a given set of canonical data $(\bar{r}, \theta = 0, p_{\bar{r}}, p_{\theta})$, we traced the (anti)neutrinos back from the rotational axis to the equatorial plane where they are supposed to be produced. The parameter ω_0 was set to an arbitrary value, e.g. $0.9c$, and the condition of the vanishing angular momentum, $L = 0$, gives the trajectories that intersect the rotational axis.

With these values for the constants of motion we can determine the magnitude of $p_{\bar{r}}$ from the norm $\mathbf{p} \cdot \mathbf{p} = 0$, and we have a consistent set of canonical data at the axis for a given p_{θ} . Since Eq. (20) determines the relation between p_{θ} and the collision angle θ_{ν} , the ray tracing code can provide the radius \bar{R} at which a null particle hitting the axis at a given radius \bar{r} and with a given collision angle left the surface of the disk in the equatorial plane.

APPENDIX C: PHYSICAL PARAMETERS OF NEUTRON AND QUARK STARS

Here we present all the data for the physical parameters of the compact stars with total mass $M \approx 1.8M_{\odot}$, and different rotational frequencies, which were obtained by the RNS code. In the Tables ρ_c is the central density, M is the gravitational mass, M_0 is the rest mass, R_e is the circumferential radius at the equator, Ω is the angular velocity, Ω_p is the angular velocity of a particle in circular orbit at the equator, T/W is the rotational-gravitational energy ratio, J is the angular momentum, I is the moment of inertia, Φ_2 gives the mass quadrupole moment, h_+ is the height from the surface of the last stable co-rotating circular orbit in the equatorial plane, h_- is the height from surface of the last stable counter-rotating circular orbit in the equatorial plane, Z_p is the polar redshift, Z_b is the backward equatorial

redshift, Z_f is the forward equatorial redshift, ω_c/Ω is the ratio of the central value of the potential ω to Ω , r_e is the coordinate equatorial radius, and r_p/r_e is the axes ratio (polar to equatorial), respectively.

We have obtained R_{in} from the formula $R_{in} = R_e + h_+$, i.e., as a the sum of the stellar radius in the equator and the height from the surface of the last stable co-rotating circular orbit in the equatorial plane. Thus the inner edge of the accretion disk is located at the radius of the innermost stable circular orbit r_{ms} , or at the equatorial radius R_e of the stellar surface, if h_+ is zero. For the RMF stiff, STOS0, Q and CFL150 type EOS the code could not provide a physically reasonable values for h_+ , and we have used a truncated form of the analytical approximation given by (Shibata & Sasaki 1998),

$$r_{ms} \approx 3r_g \left(1 - 0.54433a_* - 0.22619a_*^2 + 0.17989Q_2 - 0.23002a_*^3 + 0.26296a_*Q_2 - 0.29693a_*^4 + 0.44546a_*^2Q_2 \right), \quad (C1)$$

where $a_* = cJ/GM^2$ and $Q_2 = c^4\Phi_2/G^2M^3$ are the dimensionless spin parameter and the dimensionless mass quadrupole moment, defined in terms of the spin angular momentum J and the mass quadrupole moment Φ_2 . The results were checked by calculating the zeros of the second order derivative of the effective potential V with respect to the radial coordinate. For the calculation we applied a polynomial fit of the metric components in the equatorial plane, and computed the first and the second order derivatives of the polynomials, both analytically and numerically. Since the analytic forms of the derivatives of the polynomial fit were proved to be a good fit for the numerical derivatives too, we could use them to calculate $V_{,rr}$. The zeros of $V_{,rr}$ were in an agreement with the results of Eq. (C1) within 10%.

REFERENCES

- Akmal, A., Pandharipande, V. R., & Ravenhall, D. G. 1998, Phys. Rev. C, 58, 1804
- Alford, M. G., Rajagopal, K., & Wilczek, F. 1999, Nucl. Phys. B, 537, 433
- Alford, M. G., Rajagopal, K., Schaefer, T., & Schmitt, A. 2008, Rev. Mod. Phys., 80, 1455
- Asano, K. & Fukuyama, T. 2000, Astrophys. J., 531, 949
- Asano, K. & Fukuyama, T. 2001, Astrophys. J., 546, 1019
- Asano, K. & Iwamoto 2002, Astrophys. J., 581, 381
- Baldo, M., Bombaci, I., & Burgio, G. F. 1997, Astron. Astrophys., 328, 274
- Bardeen, J. M., Press, J. H., & Teukolsky, S. A. 1972, Astrophys. J., 178, 347

ρ_c [10^{15} g/cm ³]	1.4250	1.4200	1.4100	1.4000	1.3900	1.3800	1.3700	1.3400	1.3200	1.2940
M [M_\odot]	1.8019	1.8015	1.7992	1.7989	1.7998	1.8043	1.8076	1.8022	1.8054	1.8071
M_0 [M_\odot]	2.0701	2.0689	2.0649	2.0632	2.0627	2.0664	2.0687	2.0582	2.0589	2.0570
R_e [km]	11.2738	11.2942	11.3274	11.3734	11.4277	11.5055	11.5771	11.7052	11.8398	12.0091
Ω [10^3 s ⁻¹]	0.5246	1.0481	1.5119	2.0268	2.5064	3.0834	3.5030	4.0075	4.5071	4.9978
Ω_p [10^3 s ⁻¹]	12.8662	12.7900	12.6968	12.5925	12.4873	12.3606	12.2508	12.0334	11.8445	11.6131
T/W [10^{-2}]	0.0329	0.1317	0.2764	0.5016	0.7753	1.1888	1.5535	2.0921	2.7103	3.4355
cJ/GM_\odot^2	0.1109	0.2219	0.3208	0.4324	0.5385	0.6710	0.7707	0.8909	1.0198	1.1535
I [10^{45} g cm ²]	1.8570	1.8611	1.8651	1.8749	1.8883	1.9126	1.9336	1.9538	1.9885	2.0283
Φ_2 [10^{42} g cm ²]	0.7995	3.0606	6.3866	11.5847	17.9592	27.6936	36.3965	49.5047	64.8507	83.3478
h_+ [km]	4.3861	4.0805	3.7865	3.4791	3.2005	2.8939	2.6645	2.2884	1.9918	1.6754
h_- [km]	4.9786	5.2653	5.4976	5.7775	6.0495	6.4120	6.6746	6.8938	7.1985	7.4826
Z_p	0.3761	0.3761	0.3753	0.3755	0.3762	0.3787	0.3806	0.3788	0.3807	0.3820
Z_f	0.3390	0.3021	0.2690	0.2334	0.2006	0.1623	0.1342	0.0969	0.0620	0.0263
Z_b	0.4137	0.4516	0.4847	0.5234	0.5607	0.6087	0.6446	0.6837	0.7287	0.7737
ω_c/Ω	0.5987	0.5981	0.5965	0.5954	0.5946	0.5948	0.5947	0.5901	0.5888	0.5865
r_e [km]	8.4046	8.4247	8.4604	8.5045	8.5543	8.6196	8.6815	8.8138	8.9366	9.0959
r_p/r_e	0.9989	0.9955	0.9906	0.9830	0.9738	0.9600	0.9479	0.9300	0.9097	0.8860

Table C1. The physical parameters for a neutron star model with a DH type EOS, a total mass of $1.8M_\odot$ and angular velocities from $5 \times 10^2 \text{ s}^{-1}$ to $5 \times 10^3 \text{ s}^{-1}$.

ρ_c [10^{15} g/cm ³]	1.2640	1.2745	1.2710	1.2650	1.2500	1.2400	1.2200	1.2130
M [M_\odot]	1.7788	1.7972	1.7996	1.8019	1.8038	1.8060	1.8000	1.8083
M_0 [M_\odot]	2.0746	2.0988	2.1006	2.1016	2.1013	2.1016	2.0895	2.0976
R_e [km]	10.9336	10.9627	11.0009	11.0542	11.1299	11.2026	11.3140	11.4073
Ω [10^3 s ⁻¹]	1.5271	2.0791	2.5175	3.0120	3.5665	4.0060	4.5288	4.9377
Ω_p [10^3 s ⁻¹]	13.3079	13.2923	13.2144	13.1141	12.9808	12.8637	12.6656	12.5504
T/W [10^{-2}]	0.2913	0.5373	0.7936	1.1478	1.6342	2.0917	2.7466	3.3127
cJ/GM_\odot^2	0.3215	0.4459	0.5438	0.6564	0.7860	0.8928	1.0189	1.1312
I [10^{45} g cm ²]	1.8505	1.8847	1.8985	1.9152	1.9369	1.9586	1.9772	2.0134
Φ_2 [10^{42} g cm ²]	6.7680	12.4757	18.4095	26.6997	38.1889	49.1323	64.9632	79.0479
h_+ [km]	3.9923	3.8447	3.6152	3.3529	3.0510	2.8164	2.4695	2.2982
h_- [km]	5.7258	6.2159	6.4911	6.8003	7.1428	7.4236	7.6828	8.0085
Z_p	0.3901	0.3980	0.3996	0.4014	0.4033	0.4052	0.4042	0.4086
Z_f	0.2844	0.2532	0.2244	0.1918	0.1550	0.1258	0.0886	0.0623
Z_b	0.4993	0.5495	0.5847	0.6253	0.6717	0.7102	0.7524	0.7944
ω_c/Ω	0.5814	0.5876	0.5878	0.5878	0.5874	0.5870	0.5834	0.5848
r_e [km]	8.0918	8.0847	8.1153	8.1599	8.2259	8.2888	8.4026	8.4738
r_p/r_e	0.9907	0.9830	0.9750	0.9640	0.9490	0.9350	0.9150	0.8980

Table C2. The physical parameters for a neutron star model with APR EOS, a total mass of $1.8M_\odot$ and angular velocities from $1.5 \times 10^3 \text{ s}^{-1}$ to $5 \times 10^3 \text{ s}^{-1}$.

$\rho_c [10^{15} \text{g/cm}^3]$	3.4000	3.2000	3.1000	3.0000	2.9000	2.7000	2.5000	2.3500	2.1800	2.1500
$M [M_\odot]$	1.7891	1.7925	1.7946	1.7976	1.8002	1.8018	1.8006	1.8003	1.8067	1.8049
$M_0 [M_\odot]$	2.1026	2.1073	2.1098	2.1130	2.1155	2.1159	2.1118	2.1083	2.1107	2.1077
$R_e [\text{km}]$	9.3362	9.4389	9.4986	9.5670	9.6384	9.7808	9.9380	10.0843	10.3195	10.3498
$\Omega [10^3 \text{s}^{-1}]$	0.5525	1.0536	1.5232	2.0716	2.5101	3.0357	3.5133	4.0414	4.9989	5.0398
$\Omega_p [10^3 \text{s}^{-1}]$	17.0064	16.6910	16.4982	16.2884	16.0871	15.7139	15.3184	14.9718	14.4799	14.4116
$T/W [10^{-2}]$	0.0202	0.0764	0.1633	0.3095	0.4659	0.7178	1.0182	1.4153	2.3168	2.3808
cJ/GM_\odot^2	0.0873	0.1702	0.2490	0.3435	0.4221	0.5237	0.6215	0.7317	0.9427	0.9536
$I [10^{45} \text{g cm}^2]$	1.3887	1.4195	1.4368	1.4572	1.4781	1.5160	1.5547	1.5912	1.6573	1.6629
$\Phi_2 [10^{42} \text{g cm}^2]$	0.3292	1.1571	2.4929	4.7963	7.3192	11.6367	17.0855	24.4570	41.7102	43.1197
$h_+ [\text{km}]$	6.2663	5.9751	5.7298	5.4476	5.2036	4.8317	4.4388	4.0492	3.4490	3.3853
$h_- [\text{km}]$	6.7367	6.8894	7.0655	7.2848	7.4555	7.6162	7.7352	7.9136	8.3595	8.3522
Z_p	0.5173	0.5094	0.5060	0.5032	0.5002	0.4916	0.4815	0.4748	0.4718	0.4695
Z_f	0.4779	0.4348	0.3986	0.3578	0.3245	0.2801	0.2379	0.1954	0.1257	0.1208
Z_b	0.5571	0.5859	0.6173	0.6559	0.6866	0.7186	0.7456	0.7812	0.8597	0.8604
ω_c/Ω	0.7428	0.7328	0.7276	0.7226	0.7172	0.7050	0.6912	0.6805	0.6694	0.6666
$r_e [\text{km}]$	6.4255	6.5254	6.5820	6.6451	6.7119	6.8525	7.0128	7.1580	7.3745	7.4081
r_p/r_e	0.9993	0.9975	0.9947	0.9900	0.9850	0.9770	0.9675	0.9550	0.9270	0.9250

Table C3. The physical parameters for a neutron star model with BBBAV14 EOS, a total mass of $1.8M_\odot$ and angular velocities from $5 \times 10^2 \text{s}^{-1}$ to $5 \times 10^3 \text{s}^{-1}$.

$\rho_c [10^{15} \text{g/cm}^3]$	1.9000	1.8900	1.8800	1.8700	1.8500	1.8300	1.8000	1.7500	1.7000
$M [M_\odot]$	1.8017	1.8016	1.8033	1.8049	1.8055	1.8072	1.8085	1.8014	1.7989
$M_0 [M_\odot]$	2.1170	2.1161	2.1171	2.1180	2.1169	2.1170	2.1157	2.1027	2.0949
$R_e [\text{km}]$	10.1829	10.2058	10.2378	10.2697	10.3218	10.3809	10.4664	10.5682	10.7068
$\Omega [10^3 \text{s}^{-1}]$	1.0141	1.5161	2.0785	2.5091	3.0185	3.5098	4.0696	4.4813	5.0407
$\Omega_p [10^3 \text{s}^{-1}]$	14.9378	14.8458	14.7434	14.6556	14.5239	14.3900	14.2075	13.9766	13.7052
$T/W [10^{-2}]$	0.0957	0.2150	0.4071	0.5977	0.8768	1.2028	1.6522	2.0679	2.7144
cJ/GM_\odot^2	0.1897	0.2842	0.3918	0.4757	0.5768	0.6771	0.7952	0.8832	1.0106
$I [10^{45} \text{g cm}^2]$	1.6439	1.6473	1.6567	1.6662	1.6792	1.6954	1.7173	1.7322	1.7620
$\Phi_2 [10^{42} \text{g cm}^2]$	1.8153	4.0693	7.6582	11.2359	16.5747	22.8810	31.7467	40.2724	53.8111
$h_+ [\text{km}]$	5.2697	5.0071	4.7255	4.5082	4.2300	3.9658	3.6472	3.3156	2.9369
$h_- [\text{km}]$	6.2820	6.5233	6.8101	7.0316	7.2789	7.5282	7.8059	7.9256	8.1701
Z_p	0.4478	0.4477	0.4486	0.4495	0.4497	0.4505	0.4509	0.4461	0.4441
Z_f	0.3764	0.3415	0.3036	0.2747	0.2399	0.2068	0.1686	0.1363	0.0956
Z_b	0.5209	0.5576	0.6007	0.6346	0.6744	0.7144	0.7605	0.7885	0.8337
ω_c/Ω	0.6546	0.6536	0.6531	0.6526	0.6509	0.6494	0.6469	0.6400	0.6343
$r_e [\text{km}]$	7.2806	7.3023	7.3290	7.3559	7.4037	7.4561	7.5343	7.6451	7.7814
r_p/r_e	0.9969	0.9931	0.9870	0.9810	0.9722	0.9620	0.9480	0.9350	0.9150

Table C4. The physical parameters for a neutron star model with BBBParis EOS with a total mass of $1.8M_\odot$ and angular velocities from 10^3s^{-1} to $5 \times 10^3 \text{s}^{-1}$.

ρ_c [10^{15} g/cm 3]	0.7290	0.7250	0.7200	0.7100	0.7000	0.6850	0.6670	0.6400	0.6100	0.5700
M [M_\odot]	1.8065	1.8053	1.8069	1.8062	1.8078	1.8054	1.8062	1.8000	1.7993	1.8153
M_0 [M_\odot]	2.0443	2.0421	2.0429	2.0399	2.0395	2.0336	2.0304	2.0172	2.0092	2.0173
R_e [km]	13.5283	13.5644	13.6313	13.7402	13.8690	14.0370	14.2746	14.6091	15.0696	15.9090
Ω [10^3 s $^{-1}$]	0.5335	0.9922	1.5077	2.0600	2.5368	3.0031	3.5078	4.0159	4.5104	5.0740
Ω_p [10^3 s $^{-1}$]	9.7975	9.7329	9.6510	9.5304	9.4096	9.2539	9.0579	8.7849	8.4531	7.9384
T/W [10^{-2}]	0.0679	0.2368	0.5533	1.0555	1.6387	2.3739	3.3823	4.7272	6.4613	9.2817
cJ/GM_\odot^2	0.1641	0.3065	0.4702	0.6512	0.8160	0.9849	1.1851	1.4065	1.6653	2.0742
I [10^{45} g cm 2]	2.7037	2.7147	2.7411	2.7782	2.8268	2.8824	2.9691	3.0780	3.2448	3.5927
Φ_2 [10^{42} g cm 2]	2.8764	10.1367	23.4709	44.8791	70.2820	102.8550	148.8100	212.4910	299.7310	458.3680
h_+ [km]	0.0000	0.0000	0.0000	0.0000	0.0000	0.0000	0.0000	0.0000	0.0000	0.0000
h_- [km]	0.0000	0.0000	0.0000	$-\infty$	$-\infty$	$-\infty$	$-\infty$	$-\infty$	$-\infty$	$-\infty$
Z_p	0.2852	0.2852	0.2861	0.2867	0.2880	0.2884	0.2898	0.2896	0.2905	0.2945
Z_f	0.2456	0.2118	0.1746	0.1342	0.0994	0.0641	0.0252	-0.0170	-0.0609	-0.1178
Z_b	0.3251	0.3600	0.4008	0.4453	0.4859	0.5260	0.5726	0.6205	0.6734	0.7492
ω_c/Ω	0.4748	0.4741	0.4740	0.4727	0.4720	0.4697	0.4676	0.4628	0.4584	0.4549
r_e [km]	10.6958	10.7316	10.7913	10.8947	11.0128	11.1748	11.3977	11.7252	12.1652	12.9435
r_p/r_e	0.9977	0.9920	0.9815	0.9650	0.9460	0.9225	0.8910	0.8500	0.7990	0.7200

Table C5. The physical parameters for a neutron star model with RMF stiff EOS, a total mass of $1.8M_\odot$ and angular velocities from $5 \times 10^2 \text{ s}^{-1}$ to $5 \times 10^3 \text{ s}^{-1}$.

ρ_c [10^{15} g/cm 3]	0.4800	0.4770	3.2000	0.4750	0.4700	0.4620	0.4540	0.4400	0.4230	0.3980	0.3690
M [M_\odot]	1.8061	1.8031	1.7925	1.8076	1.8086	1.8017	1.8088	1.8002	1.8039	1.8033	1.8541
M_0 [M_\odot]	2.0118	2.0070	2.1073	2.0113	2.0103	1.9990	2.0034	1.9876	1.9842	1.9725	2.0155
R_e [km]	15.2003	15.2651	9.4389	15.3585	15.5171	15.7140	16.0281	16.4469	17.1311	18.2747	21.0394
Ω [10^3 s $^{-1}$]	0.5081	1.0560	1.0536	1.5041	2.0308	2.5000	3.0348	3.5301	4.0582	4.5293	4.9020
Ω_p [10^3 s $^{-1}$]	8.2289	8.1525	16.6910	8.0845	7.9708	7.8258	7.6457	7.3877	7.0275	6.4676	5.3725
T/W [10^{-2}]	0.0865	0.3780	0.0764	0.7757	1.4473	2.2664	3.4814	5.0168	7.2439	10.3451	14.9104
cJ/GM_\odot^2	0.1891	0.3949	0.1702	0.5701	0.7835	0.9799	1.2345	1.4877	1.8274	2.2429	2.9524
I [10^{45} g cm 2]	3.2706	3.2868	1.4195	3.3309	3.3905	3.4448	3.5750	3.7037	3.9573	4.3520	5.2932
Φ_2 [10^{42} g cm 2]	4.8687	21.1326	1.1571	43.4479	81.4042	127.9780	199.1870	290.8950	432.8830	650.3940	1061.9200
h_+ [km]	$-\infty$	0.0000	5.9751	0.0000	0.0000	0.0000	0.0000	0.0000	0.0000	0.0000	0.0000
h_- [km]	1.3339	1.9240	6.8894	2.4997	3.1777	3.7552	4.5759	5.2774	6.2012	7.1106	7.8501
Z_p	0.2415	0.2416	0.5094	0.2432	0.2446	0.2448	0.2480	0.2486	0.2515	0.2529	0.2601
Z_f	0.2020	0.1596	0.4348	0.1260	0.0856	0.0481	0.0056	-0.0380	-0.0885	-0.1461	-0.2296
Z_b	0.2814	0.3251	0.5859	0.3634	0.4094	0.4504	0.5038	0.5534	0.6165	0.6842	0.7891
ω_c/Ω	0.4201	0.4194	0.7328	0.4203	0.4202	0.4183	0.4191	0.4160	0.4145	0.4099	0.4102
r_e [km]	12.3910	12.4567	6.5254	12.5372	12.6848	12.8822	13.1688	13.5832	14.2357	15.3506	18.0144
r_p/r_e	0.9970	0.9870	0.9975	0.9735	0.9510	0.9240	0.8850	0.8370	0.7700	0.6800	0.5400

Table C6. The physical parameters for a neutron star model with STOS0 EOS, a total mass of $1.8M_\odot$ and angular velocities from $5 \times 10^2 \text{ s}^{-1}$ to $5 \times 10^3 \text{ s}^{-1}$.

ρ_c [10^{15} g/cm ³]	1.0800	1.0700	1.0500	1.0300	1.0000	0.9800	0.9490	0.9310
M [M_\odot]	1.8039	1.8065	1.8032	1.8029	1.8000	1.8014	1.7999	1.8071
M_0 [M_\odot]	2.1221	2.1241	2.1176	2.1146	2.1071	2.1057	2.0989	2.1045
R_e [km]	11.2268	11.2717	11.3243	11.3914	11.4900	11.5804	11.7097	11.8329
Ω [10^3 s ⁻¹]	1.4909	2.0426	2.5022	2.9918	3.5684	3.9966	4.5072	4.9097
Ω_p [10^3 s ⁻¹]	12.8593	12.7703	12.6630	12.5507	12.3985	12.2828	12.1180	11.9932
T/W [10^{-2}]	0.3678	0.6975	1.0654	1.5517	2.2722	2.9149	3.8377	4.6703
cJ/GM_\odot^2	0.3650	0.5047	0.6224	0.7523	0.9103	1.0352	1.1904	1.3280
I [10^{45} g cm ²]	2.1519	2.1717	2.1862	2.2100	2.2420	2.2765	2.3212	2.3772
Φ_2 [10^{42} g cm ²]	10.3179	19.1974	30.1157	43.9566	64.5770	83.4277	110.8010	136.1140
h_+ [km]	0.0000	0.0000	0.0000	0.0000	0.0000	0.0000	0.0000	0.0000
h_- [km]	0.0000	0.0000	0.0000	0.0000	0.0000	0.0000	0.0000	0.0000
Z_p	0.3822	0.3837	0.3832	0.3839	0.3843	0.3859	0.3870	0.3906
Z_f	0.2775	0.2405	0.2084	0.1752	0.1355	0.1066	0.0712	0.0443
Z_b	0.4905	0.5339	0.5685	0.6080	0.6550	0.6930	0.7386	0.7805
ω_c/Ω	0.5400	0.5399	0.5374	0.5359	0.5329	0.5317	0.5289	0.5292
r_e [km]	8.3558	8.3912	8.4438	8.5041	8.5967	8.6746	8.7925	8.8900
r_p/r_e	0.9893	0.9800	0.9690	0.9549	0.9350	0.9170	0.8920	0.8700

Table C7. The physical parameters for a quark star model with Q EOS, a total mass of $1.8M_\odot$ and angular velocities from $1.5 \times 10^3 \text{ s}^{-1}$ to $5 \times 10^3 \text{ s}^{-1}$.

ρ_c [10^{15} g/cm ³]	0.7830	0.7790	0.7750	0.7670	0.7580	0.7470	0.7350	0.7200	0.7050
M [M_\odot]	1.8003	1.8000	1.8036	1.8015	1.8012	1.7994	1.8022	1.7997	1.8069
M_0 [M_\odot]	2.1162	2.1149	2.1179	2.1129	2.1098	2.1042	2.1035	2.0954	2.0986
R_e [km]	11.7280	11.7561	11.8075	11.8591	11.9321	12.0175	12.1406	12.2707	12.4636
Ω [10^3 s ⁻¹]	1.0163	1.4994	2.0421	2.5147	3.0197	3.5035	4.0415	4.5235	5.0640
Ω_p [10^3 s ⁻¹]	12.0724	12.0028	11.9281	11.8403	11.7438	11.6396	11.5143	11.3772	11.2109
T/W [10^{-2}]	0.1987	0.4351	0.8147	1.2517	1.8350	2.5197	3.4382	4.4366	5.7661
cJ/GM_\odot^2	0.2749	0.4071	0.5603	0.6944	0.8430	0.9894	1.1645	1.3263	1.5338
I [10^{45} g cm ²]	2.3770	2.3865	2.4112	2.4269	2.4533	2.4820	2.5323	2.5767	2.6619
Φ_2 [10^{42} g cm ²]	7.1160	14.9170	27.8321	42.6462	62.2833	85.5102	117.0170	151.5570	198.8980
h_+ [km]	0.0000	0.0000	0.0000	0.0000	0.0000	0.0000	0.0000	0.0000	0.0000
h_- [km]	0.0000	0.0000	0.0000	0.0000	0.0000	0.0000	0.0000	0.0000	0.0000
Z_p	0.3539	0.3545	0.3566	0.3573	0.3589	0.3604	0.3635	0.3654	0.3703
Z_f	0.2819	0.2487	0.2125	0.1803	0.1463	0.1135	0.0775	0.0441	0.0070
Z_b	0.4276	0.4641	0.5077	0.5451	0.5872	0.6285	0.6784	0.7234	0.7813
ω_c/Ω	0.5010	0.5008	0.5016	0.5008	0.5005	0.4997	0.4999	0.4988	0.4997
r_e [km]	8.8688	8.8932	8.9318	8.9796	9.0431	9.1197	9.2223	9.3399	9.4977
r_p/r_e	0.9935	0.9864	0.9750	0.9620	0.9450	0.9250	0.8990	0.8710	0.8350

Table C8. The physical parameters for a neutron star model with CFL150 EOS, a total mass of $1.8M_\odot$ and angular velocities from 10^3 s^{-1} to $5 \times 10^3 \text{ s}^{-1}$.

- Baym, G., Bethe, H. A., & Pethick, C. J. 1971, Nucl. Phys. A, 175, 225
- Baym, G., Pethick, C. J., & Sutherland, P. 1971, Astrophys. J., 170, 299
- Bhattacharyya, A., Ghosh, S. K., Mallick, R., & Raha, S. 2009, arXiv0905.3605
- Bethe, H. A. 1990, Rev. Mod. Phys., 62, 801
- Bethe, H. A. & Wilson, J. R., 1985, Astrophys. J., 295, 14
- Birkl, R., Aloy, M. A., Janka, H.-Th., & Muller, E. 2007, Astron. Astrophys. 463, 51
- Bodmer, A. R., 1971, Phys. Rev. D, 4, 1601
- Cadeu, C., Leahy D., & Morsink S. 2005, Astrophys. J., 618, 451
- Cadeu, C., Morsink S. & Leahy D. 2007, Astrophys. J., 654, 458
- Chan, T. C., Cheng, K. S., Harko, T., Lau, H. K., Lin, L. M., Suen, W. M., & Tian, X. L. 2009, Astrophys. J., 695, 732
- Cheng, K. S., Dai, Z. G., & Lu, T. 1998a, Int. J. Mod. Phys. D, 7, 139
- Cheng, K. S., Harko, T., Huang, Y. F., Lin, L. M., Suen, W. M., & Tian, X. L. 2009, JCAP, 09, 007
- Cooperstein, J., van den Horn, L. J., & Baron, E. A. 1986, Astrophys. J., 309, 653
- Cooperstein, J., van den Horn, L. J., & Baron, E. A. 1987, Astrophys. J., 321, L129
- Dai, Z. G., Peng, Q. H., & Lu, T. 1995, Astrophys. J., 440, 815
- Dey, M., Bombacci, I., Dey, J., Ray, S., & Samanta, B. C. 1998, Phys. Lett. B, 438, 123
- Douchin, F. & Haensel, P. 2001, Astron. Astrophys., 380, 151
- Feynman, R. P., Metropolis, N., & Teller, E. 1949, Phys. Rev., 75, 1561
- Goodman, J., Dar, A., & Nussinov S., 1986 Astrophys. J., 314, L7
- Horvath, J. E., & Lugones, G. 2004, Astron. Astrophys., 422, L1
- Itoh, N. 1970, Prog. Theor. Phys., 44, 291
- Kovács, Z., Cheng, K. S., & Harko, T. 2010, Month. Not. Roy. Astr. Soc., 402, 1714
- Kubis, S., & Kutschera, M. 1997, Phys. Lett. B, 399, 191
- Lugones, G., & Horvath, J. E. 2002, Phys. Rev. D, 66, 074017
- Mallick, R., & Majumder, S. 2009, Phys. Rev. D. 79, 023001
- Mészáros, P. & Rees, M. J. 1992, Month. Not. Roy. Astr. Soc., 257, 29
- Mészáros, P. 2006, Rept. Prog. Phys., 69, 2259
- Miller, W. A., George, N. D., Kheyfets, A., & McGhee, J. M. 2003, Astrophys. J., 583, 833
- Novikov, I. D., & Thorne, K. S. 1973, in Black Holes, ed. C. DeWitt and B. DeWitt, New York: Gordon and Breach
- Nozawa, T., Stergioulas, N., Gourgoulhon, E., & Eriguchi, Y. 1998, Astron. Astrophys.,

132, 431

Page, D. N., & Thorne, K. S. 1974, *Astrophys. J.*, 191, 499

Paczynski, B. 1990, *Astrophys. J.*, 363, 218

Pandharipande, V. R. 1971, *Nucl. Phys. A*, 178, 123

Perez-Giz, G., Levin, J., 2009, *Phys. Rev. D*, 79 124014

Rapp, R., Schaffer, T., Shuryak, E. V., & Velkovsky, M. 2000, *Ann. Phys. (N. Y.)*, 280, 35

Ruffert, M. & Janka, H.-T. 1998, *Astron. Astrophys.*, 338, 535

Ruffert, M. & Janka, H.-T. 1999, *Astron. Astrophys.*, 344, 573

Salmonson, J. D. & Wilson, J. R., 1999, *Astrophys. J.*, 517, 895

Salmonson, J. D. & Wilson, J. R., 2001, *Astrophys. J.*, 561, 950

Shen, H., Toki, H., Oyamatsu, K., & Sumiyoshi, K. 1998, *Nucl. Phys. A*, 637, 435

Shibata, M., & Sasaki, M. 1998, *Phys. Rev. D*, 58, 104011

Stergioulas, N., & Friedman, J. L. 1995, *Astrophys. J.*, 444, 306

Stergioulas, N., Kluzniak, W., & Bulik, T. 1999, *Astron. Astrophys.*, 352, L116

Stergioulas, N. 2003, *Living Rev. Rel.*, 6, 3

Witten, E. 1984, *Phys. Rev. D*, 30, 272

Zhang, B. 2007, *Chin. J. Astron. Astrophys.*, 7, 1

Zhang, D. & Dai, Z. G. 2009, *Astrophys. J.*, 703, 461

This paper has been typeset from a \TeX / \LaTeX file prepared by the author.

